

TECHNICAL UNIVERSITY OF CRETE  
SCHOOL OF ELECTRONIC AND COMPUTER ENGINEERING



# Self-Powered Plant Sensor for Scatter Radio

by

Christos Konstantopoulos

A THESIS SUBMITTED IN PARTIAL FULFILLMENT OF  
THE REQUIREMENTS FOR THE M.Sc. DEGREE ON  
ELECTRONIC AND COMPUTER ENGINEERING

March 2015

## THESIS COMMITTEE

Assistant Professor Koutroulis Eftychios, *Thesis Supervisor*

Associate Professor Aggelos Bletsas

Associate Professor Antonios Deligiannakis

# Abstract

In agriculture applications (e.g. greenhouses, vineyards etc.) it is required to automatically gather information about environmental variables such as soil and air humidity, as well as temperature in the vicinity of plants within the same field, with low-cost and high-scalability. Thus, sensor networks that are extending over a broad area and gather environmental data for microclimate monitoring, are indispensable for the application of optimal crop management techniques. The field of plant electro-physiology investigates the correlation of environmental variables with the electrical signals that are produced by diverse types of plants. Existing research in measurement of electrical signals generated by plants has been conducted using high-cost equipment, such as laboratory multi-meters and data-loggers, in order to perform the signal-conditioning and data acquisition operations required. This thesis introduces for first time in the existing research literature a novel low cost and self-powered sensor node that belongs to a large-scale scatter radio network and simultaneously is powered in a parasitic way to the plants, as well as is able to acquire and transmit these types of signals from each plant. Furthermore, in the context of this thesis, several experimental prototypes of the proposed node were developed, as well as used to gather measurements of electrical signals that are generated from multiple Avocado plants. The experimental results demonstrate the successful operation of the proposed WSN node, as well as indicate the correlation of plants signals with solar irradiation and plant irrigation events. Thus, the proposed system can be employed in precision agriculture applications for automated irrigation scheduling, control of the plant ambient conditions etc. based on data derived directly by the plants.

# Acknowledgements

I would like to take this opportunity to wholeheartedly thank my advisor, professors, colleagues, family and dear friends. This thesis was made possible only through the support and guidance they offered. I would like to extend my sincerest thanks to my advisor and mentor Eftychios Koutroulis, who has offered me all the guidance I needed and facilitated my academic growth, throughout my course as a graduate student. His patience, time and advice are precious to me. Special thanks are also due to my excellent professors and colleagues. Specifically, I would like to thank professors Aggelos Bletsas who introduced me to the world of wireless sensor networking and who helped me to further explore exciting aspects such as analogue scatter radio principles. Moreover, special thanks to Dr. Nikolaos Mitainoudis who contributed to the signal processing of the plant signals and the correlation with environmental stimuli. Moreover, I owe to the members of the Electric Circuits & Renewable Energy Sources and Telecommunications Laboratories of the Technical University of Crete for their technical assistance whenever it was needed. Their support is acknowledged. Finally, I would like to thank my friends and family for the invaluable moral support they provided. My parents, brother deserve mention, although I couldn't possibly write enough. This work was supported by the ERC-04-BLASE project, executed in the context of the "Education & Lifelong Learning" Operational Program of the National Strategic Reference Framework (NSRF), General Secretariat for Research & Technology (GSRT), funded through European Union-European Social Fund and Greek national funds.

# Table of Contents

# List of Figures

# List of Tables

# Chapter 1

## Introduction

The investigation of the micro-climate dynamics of crops have been the center of recent scientific research [? ]. Wireless Sensor Networks (WSNs) have been deployed for performing wireless monitoring of environmental parameters, such as humidity, temperature and soil moisture, in critical points of a crop field, since sensing these parameters over a broad area offers the ability to perform a precise analysis of the generated micro-climate conditions [? ? ? ]. Consequently, each agricultural area may be treated individually by assessing its individual needs, thus achieving optimal management of nutrient resources and maximization of the crops growth rate. In this context, several research works have demonstrated that plants respond to changes of light, pH, temperature and minerals by deploying certain intracellular processes [? ? ? ]. The field of electro-physiology has contributed towards the correlation of these responses with electrical signals that are generated by the plants. Particularly, it has been shown that several plants exhibit significant electrical response which is correlated with the acquisition of nutrients [? ]. Moreover, several research works have demonstrated that correlation exists between the electrical signals generated by the plants with external stimuli, such as pollination, watering, wounding and temperature variations [? ? ? ].

The existing technology of WSNs provides high cost and high power consumption solutions that it are not capable to cover the requirements of precision agriculture schemes which require to continuously monitor the electrical signals of multiple plants within an extended area of a crop field. Thus, present scientific research has been limited to small-scale experimentation, performed within the laboratory environment. Although several works have presented Radio Frequency IDentification (RFID) sensor nodes that acquire and transmit biological electrical signals, such as those produced by ElectroEncephaloGraphy (EEG) and Electro-CardioGraphy (ECG) procedures [? ? ] none of them has yet been focused on

the measurement and wireless transmission of the electrical signals generated by plants. Additionally, the electrical signals produced by the plant have not yet been exploited for simultaneously power-supplying the devices which are also used for their measurement and/or wireless transmission. In this work, with the purpose to tackle all these constraints, a low-cost fully-autonomous wireless sensor node is presented. This novel node is capable to: measure the electro-physiological signal generated by a plant, achieve a self-powered operation by harvesting energy from the plant under supervision and transmit wirelessly the acquired measurements to a central data-acquisition unit using analogue backscatter-radio principles, thus achieving low power consumption and long communication range.

## 1.1 Energy harvesting in Wireless Sensor Networks

Energy harvesting schemes are quite attractive in Wireless Sensor Networks. Several works have demonstrated nodes that are able to harvest the ambient energy with aim to achieve perpetual operation. These schemes extend the life time of the WSN as well as, due to the fact that the self-sustainable wireless sensor nodes are mainly based in battery-less architectures, which utilize capacitors for energy storage, the maintenance cost is minimized [? ]. Solar, kinetic, ambient RF as well as the thermoelectric energy conversion are the most commonly used forms of sustainable energy that have been exploited for powering Wireless Sensor Nodes [? ? ? ]. However, hindrance of exploiting these forms of energy sources arises in real agricultural environments where they are either scarce (ambient RF energy) or they are not available all along the day (solar, kinetic energy, thermoelectric conversion). In order to tackle these constraints, one option is to accumulate the excess energy that is harvested during operation in order to exploit it when the energy source diminishes [? ? ? ]. Moreover, other designs operate with duty cycle control in case that the available power level is inadequate for operation but is consistently available [? ? ].

Major issues of power management schemes constitute the cold-start operation, as well as the maximum power point transfer between the energy source and the

Power Management Unit. In case that the node suffers a complete drainage of energy, the essential subsystems that control the main power converter are unable to operate. Under these circumstances, the power management units employ starter circuits that wake-up the internal PMU circuitry. These starter schemes commonly employ motion-assisted, oscillation-driven positive feedback amplifier circuits that step-up the input voltage to a level that the main control unit operates [? ? ? ? ? ]. Moreover, Maximum Power Point Tracking procedures tracks the energy source's maximum power point under varying environmental conditions. The MPPT procedure that varies the energy source's load adaptively is implemented either by utilizing Digital Signal Processing hardware or analog hardware [? ? ? ]. Its method is chosen according to the available input energy, however, in case that the incoming power is ultra low ( $<10\mu\text{W}$ ) the impedance matching is static and predetermined by the designer, taking into account the source's power-voltage characteristic curve.

## 1.2 Electrical behaviour of plants

Several works have demonstrated that correlation exists between the electrical signals of plants and external stimuli. Specifically, the electrical response of plants is associated with pollination, watering, wounding and temperature changes. During these triggering events, Action Potentials (AP) and Variation Potentials (VP), which are the two main types of relevant electrical signals, are induced across the stem of the plants [? ? ? ]. These types of signals are induced shortly after the stimulative action and may either pertain an "all or nothing" type of response (AP electrical signals), or vary in amplitude and range depending on the intensity of the stimulus (VP electrical signals)[? ? ]. Figure ?? presents examples of the electrical signals that are generated across the leaf petiole under cooling and wounding stimuli. The VP signal that is generated by cooling is shown in Fig.?.?. As illustrated, the response spans for about 10s where the potential goes as high as about  $140\text{ mV}$  and gradually fades. On the other hand, Fig. ??(b) indicates the plant's response that is caused due to wounding. The stimuli resulted in a response that fluctuates for about  $50\text{ mV}$  and spans for 12 s. Figure ?? illustrates the average values of electrical signals belonging to 7 plants for 4 consecutive days, as well as

its response to irrigation events for 2 different configurations of the electrodes [? ].

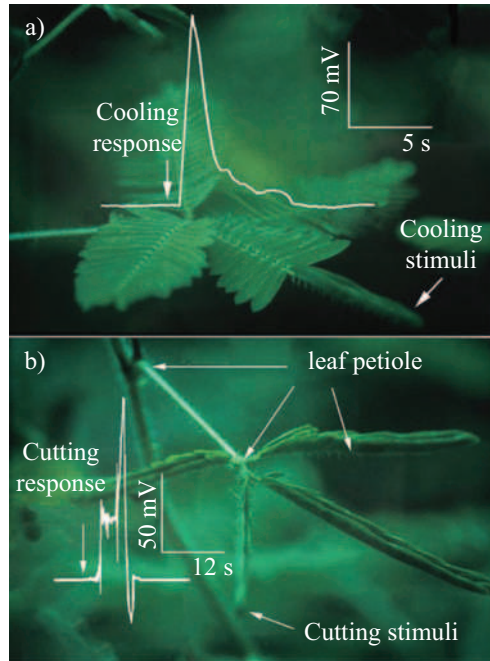


Figure 1.1: AP and VP signals in Mimosa pudica plant [? ].

Furthermore, apart from the response at the spontaneous stimuli, several plants have demonstrated significant electrical response that is correlated with the soil water availability [? ? ? ]. Figure ?? as is presented illustrates the daily electrical response of maize plant to water availability [? ]. As denoted, the electric potential follows the trend of water availability into the soil. After 96 hours, in the moment that the plant gets irrigated, an AP varying signal appears and the electrical signal starts to decrease following the inclination of soil moisture. As the soil moisture stabilizes, the plant electrical potential stabilizes as well.

### 1.3 The Proposed Self-Powered Sensor Node

In this thesis, an integrated WSN node is introduced for monitoring the physiology of plants, where the plant itself is employed to operate simultaneously as a sensing element and as an electric energy source, with an incorporated radio

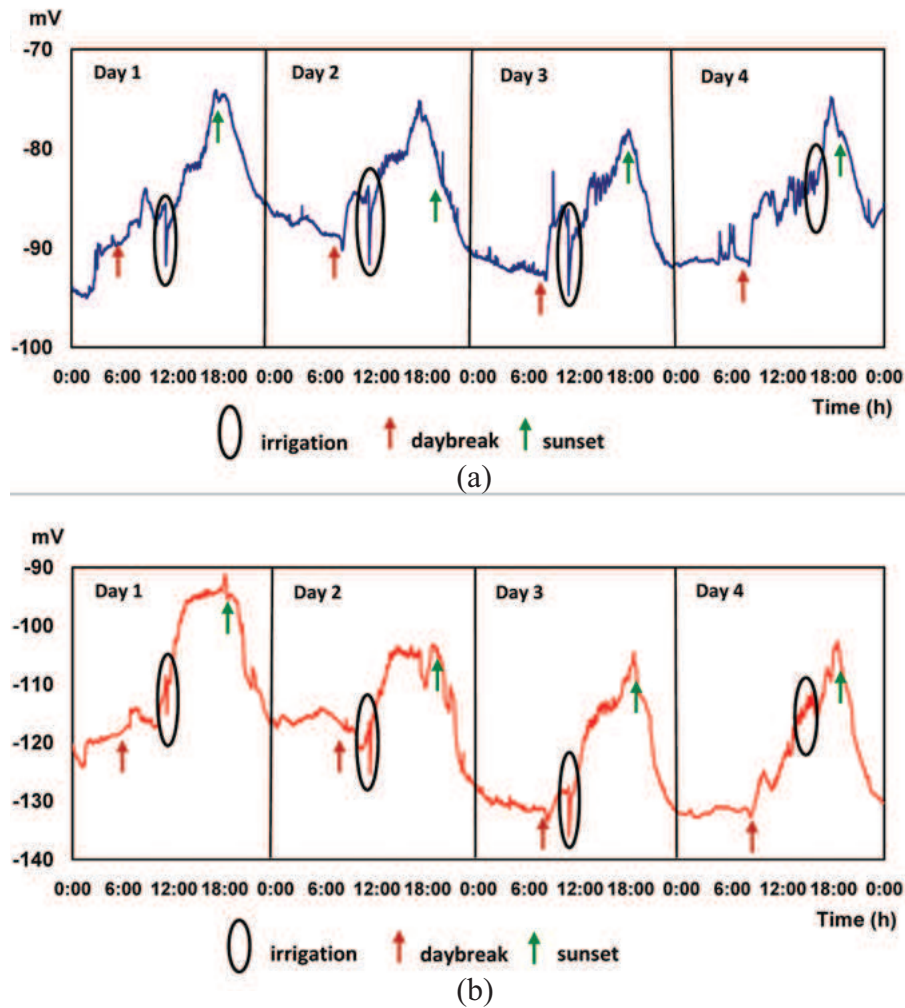


Figure 1.2: Daily rhythm of the electrical potential difference in avocado plants. Systematic act of irrigation is performed. Micro electrodes are inserted at 25 (a) and 85 (b) cm above the soil surface.

data-transmission capability. The proposed system is capable to: (i) measure the electrical signal generated by a plant, (ii) transmit the acquired information through an ultra-low-power analogue backscatter communication link over a relatively long range and (iii) cover its power-supply requirements by harvesting the biological energy produced by the same the plant under monitoring. It is the first time in the existing research literature that a wireless sensing module is presented, which enables the implementation of precision agriculture schemes where

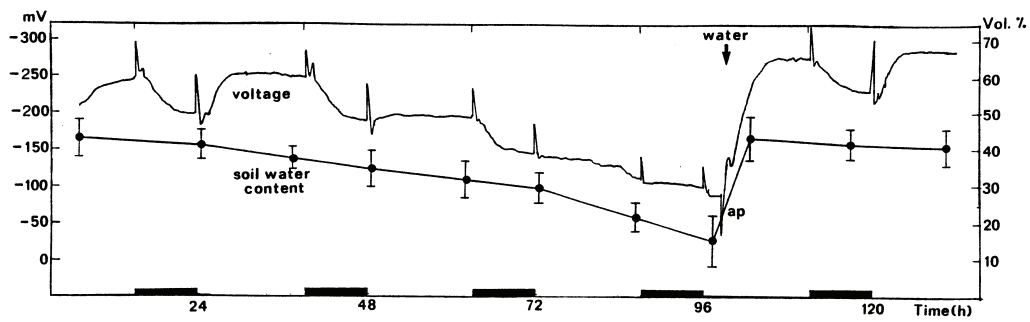


Figure 1.3: Daily rhythm of the electrical potential difference in maize plants during soil drying [? ]. The irrigation event is indicated after 96 hours from the start of measurements.

the electrical signals generated by each plant of a crop field are centrally monitored through a low-cost, large-scale and fully-autonomous WSN. Thus, by supervising the physiology of the individual plants, their needs may be optimally assessed and gratified.

## Chapter 2

# Plant Signal Acquisition Network

A large-scale Wireless Sensor Network that is able to cover the needs of sensing the electrical signals of plants at a remote field should be characterized by the low cost and high scalability. A communication radio scheme that fulfils these requirements is the analogue bistatic backscatter communication architecture [? ], which deploys a radio emitter dislocated from the reader [? ] (bistatic configuration). A backscattering bistatic network constitutes a wireless sensor network that senses and collects environmental variables by exploiting the backscattering communication principle. In contrast to other communication architectures, it offers long range communication capability and low power consumption. The communication is achieved by the analogue frequency modulation of the sensed information. Also, Frequency Division Modulation Access control is deployed as a channel access method. Several works have demonstrated RFID sensor nodes that acquire and transmit biological signals [? ? ? ]. This work presents a backscatter sensor that is capable to acquire the plant biological signals with analogue backscatter communication, which offers less receiver software complexity in contrast to the existing environmental sensing implementations.

The WSN architecture is depicted in Fig. ?? . The central emitter transmits the carrier that is modulated by each node in way that the sensed information dictates. The modulated carrier is collected and demodulated by the reader. As Fig. ?? illustrates, each node constitutes a module that senses the electrical signals across the plant's stem by the signal conditioner that it encloses. The conditioned signal controls a voltage controlled oscillator that generates the modulation signal. The RF front-end includes a specified layout design that maximizes the backscattering efficiency, as well as the switching transistor which modulates the incident carrier.

With the purpose of reassuring seamless communication among the WSN nodes, the FDMA protocol was employed. It reserves the adequate bandwidth for each

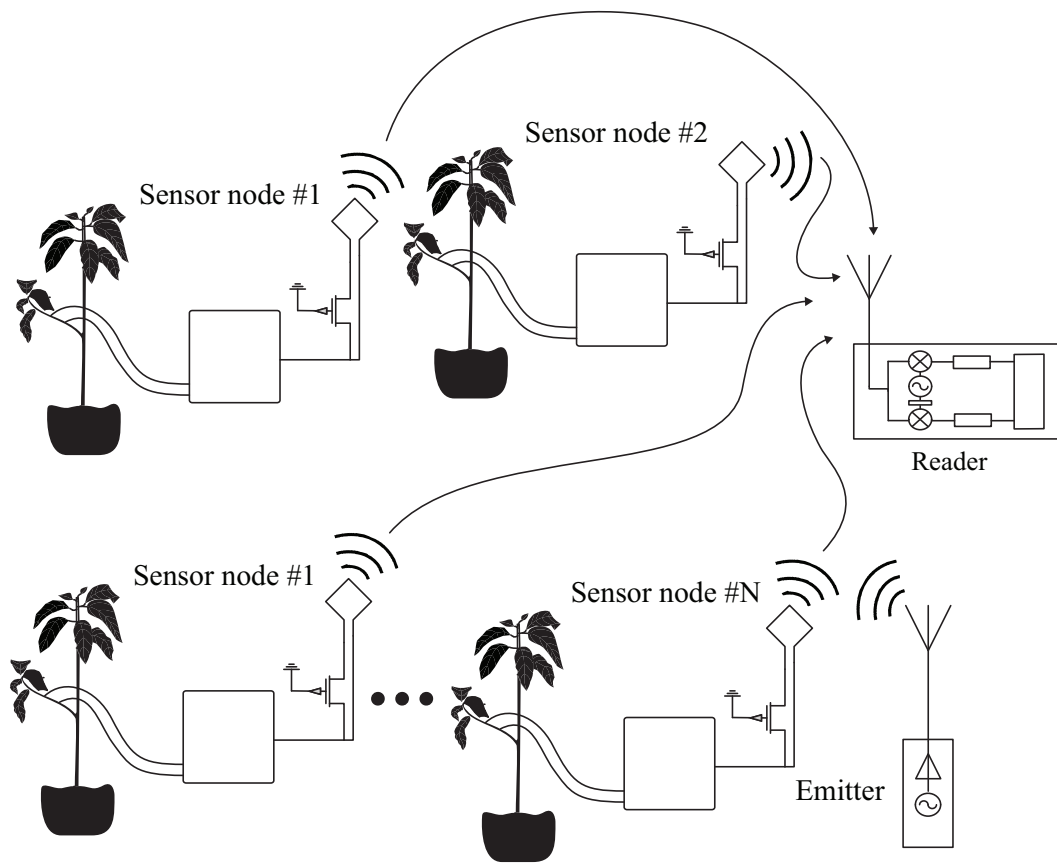


Figure 2.1: The architecture of the WSN for acquiring the signals generated by multiple plants.

node in order to transfer its sensed information. As Fig. ?? illustrates, each node WSN occupies a predefined spectral band. In case that the input of WSN nodes is outside the predefined range, a specific bandwidth is allocated with an aim to avoid collisions between any adjacent nodes.

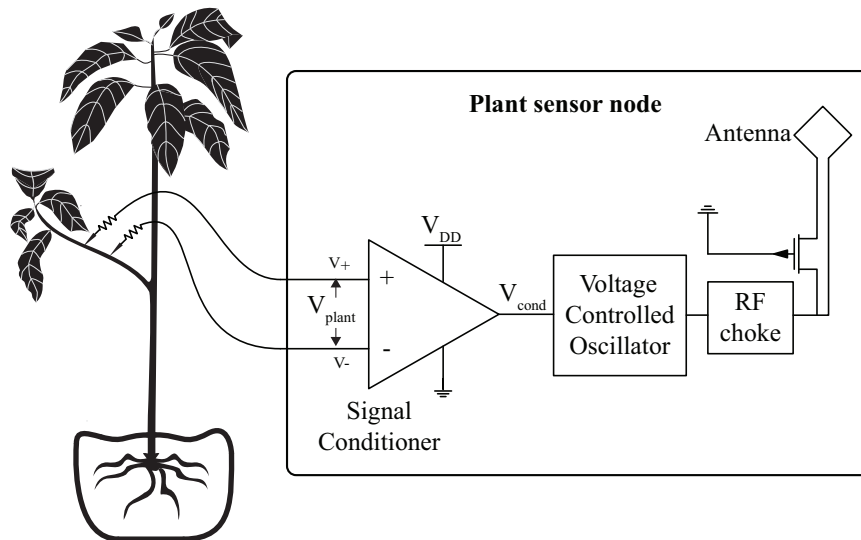


Figure 2.2: A block diagram of the sensor node that collects and scatters back the modulated signal that contains the plant signal information.

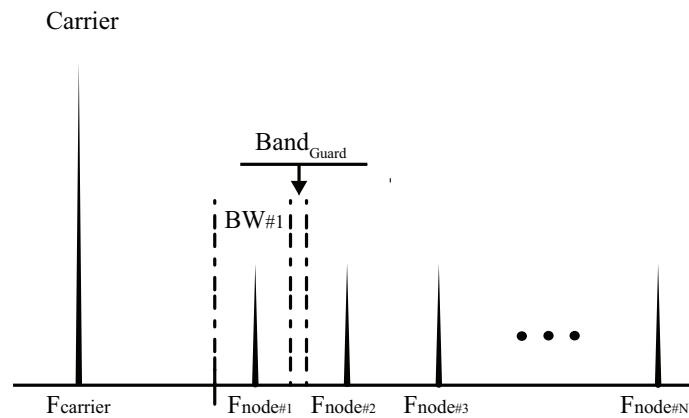


Figure 2.3: An example of the frequency division medium access scheme of multiple WSN nodes transmitting simultaneously.

## 2.1 Plant signal acquisition

The signal acquisition unit that interfaces the weak bio-potentials that are generated by biological sources should be characterized by high common-mode and differential-mode input impedance [? ]. The plant's electrical signals can be classified as the upper bound of the bio-electrical signals, with a magnitude higher than the ElectroCardioGraphy (ECG) signals. Therefore, there is no need of exquisite amplifiers that amplify ultra low bio-potentials. The plant voltage is measured using Ag pin electrodes, inserted into the plant stem or branch, having the advantage of achieving long-term stability, without performance degradation. Alternatively, glass pipettes containing Ag/AgCl wires and KCl may also be attached on the plant stem or branch [? ], but they are in need of periodical calibration process. Also, the solution that employs the Ag/AgCl wires in agar enriched with KCl, which have been utilized in [? ? ? ], may exhibit performance degradation after long-term usage, due to evaporation of the water contained in the agar.

The triple op-amp Instrumentation Amplifier topology is widely used in the ECG level of signal measurement applications. The major characteristic of IA module is the extremely high input impedance that the non-inverting closed-loop configuration of the input operational amplifiers offers [? ]. In the same time the differential amplifier with resistors that insure a perfect balanced bridge preserves high common mode rejection ratio that is crucial for the application. Furthermore, an auxiliary fourth op-amp was employed to adjust the offset at the output voltage in order to allocate the nodes in different frequency bands. Due to the low output impedance of op-amp, a bridge disturbance is being prevented. Figure ?? depicts the main IA's circuitry. With the purpose to reassure a perfect matched bridge, the module should be consisted of operational amplifiers with low offset current and voltage. Moreover, considering the low level signals that the input buffers interfaces, the input bias current should be below 100pA. After an extensive literature search, it was concluded that the operational amplifier of IC's family MCP603x [? ] meet the demand of low voltage offset, ultra low power consumption and low input bias current characteristics. The MCP603x op-amp family set constraints on the maximum and minimum allowed common voltage level. In order to set a constant common voltage that is not disturbed either by the plant

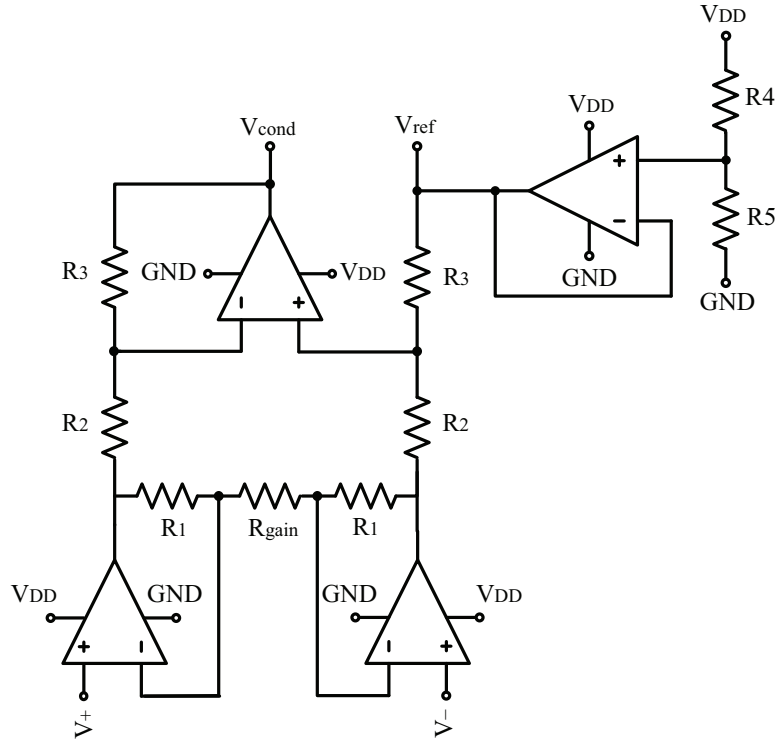


Figure 2.4: Instrumentation amplifier circuitry.

electrical characteristics, or possible electrical coupling between the environment and the wireless node, the  $V_-$  pin was connected to the reference voltage.

The cable that extrudes from the node's main compartment tends to be susceptible to ambient noise. In order to minimize the noise pick-up, as well as the ground-loop interference, a cable of shielded twisted pair was used to transfer the signal. Both wires pick-up identical noise that appear as a common-mode component and are practically eliminated by the IA module's high common mode rejection. Additionally, with a view to minimize the interference of the ambient environmental noise with the twisted pair, the cable's braid shield is being driven by the reference voltage. Figure ?? illustrates the assembly of the instrumentation amplifier accompanied with the cable attached on the plant's stem.

Equation ?? refers to the calculation of the  $V_{cond}$  output according to the  $V_+ - V_-$  input.

$$V_{cond} = G * (V_+ - V_-) + V_{ref} \quad (2.1)$$

The input gain, as well as the voltage reference  $V_{ref}$ , are calculated by Eq. ?? and Eq. ??, respectively.

$$G = \left(1 + 2 * \frac{R_1}{R_{gain}}\right) * \frac{R_3}{R_2} \quad (2.2)$$

$$V_{ref} = V_s * \frac{R_4}{R_5 + R_4} \quad (2.3)$$

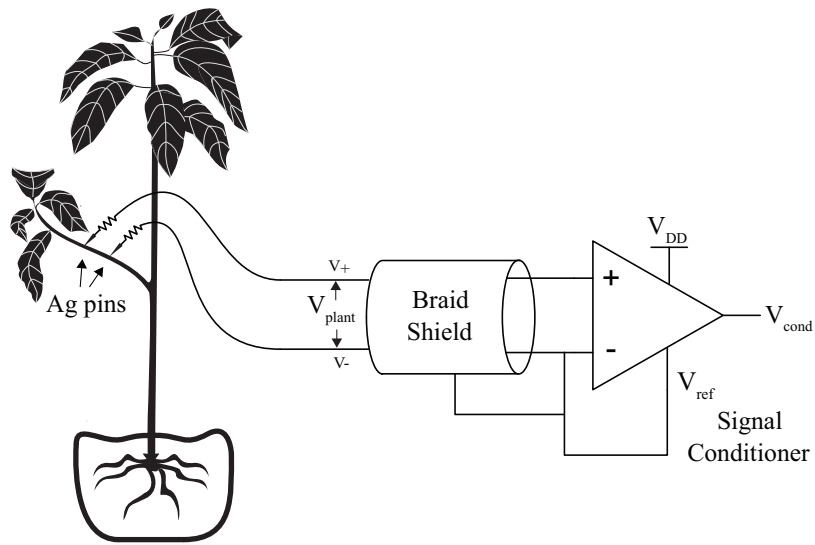


Figure 2.5: Signal conditioning interface.

## 2.2 FM modulation

The analog backscattering node that interfaces the plant analogue signals was designed with the purpose to constitute a scalable analogue backscattering architecture that can support a large amount of wireless nodes. Although several examples of analogue backscatter sensor networks have already been demonstrated [? ? ], their scalability is quite constrained. In order to outstrip this hindrance it was imperative to modulate the carrier with a much higher frequency span that, in consequence, offers wider usable spectrum to allocate the nodes. The voltage controlled oscillator performs the operation of frequency modulation according to the amplitude of the conditioned signal. The oscillation unit is based on the advanced TS3002 commercial IC timer [? ] that is about 60 times more power efficient compared to the ICM7555 timer at the same cost. In the same time, it offers a wide frequency band generation capability (5 kHz to 290 kHz) with remarkable linear response. Figure ?? illustrates the timer configured as a voltage controlled oscillator accompanied with the RF front-end. The incoming signal is frequency modulated by the TS3002 IC timer as the level of  $V_{cond}$  signal dictates. The squared-wave signal that is produced, switches the RF Mosfet transistor (BF1118).

The operation of the backscattering modulator is based on switching the termination load of the antenna between two different states. When the switching transistor is at the on-state, the incoming carrier signal is reflected by the antenna and scattered back to the reader with (ideally)  $180^\circ$  phase-difference. During the off-state of the switching transistor, the received signal is reflected back to the reader with (ideally) zero phase. A choke is used to decouple the incoming wave from the control circuit of the transistor. As a result of the modulation process the node's sub-carrier appears on the reader's periodogram on both sides of the center carrier at frequency  $F_{carrier} \pm F_{sw}$  [? ].

According to the datasheet of the TS3002 IC the oscillation frequency in case that a zero voltage is applied at  $R_{set}$ , is given by the equation Eq. ??.

$$F_{sw} = \frac{1}{1.19 * R_{total} * C_{set}} \quad (2.4)$$

The maximum and minimum oscillation points are derived according to Eq. ??

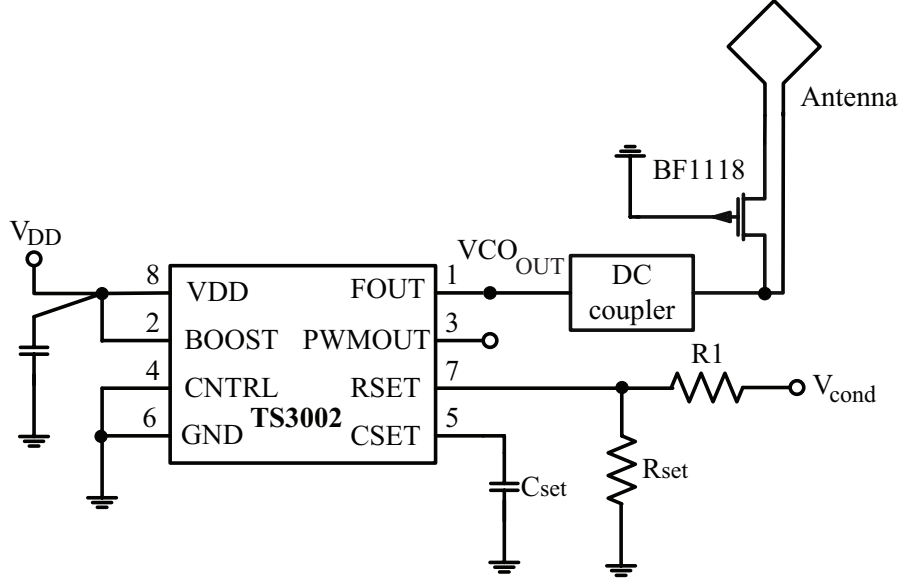


Figure 2.6: Voltage controlled oscillator and RF-front end circuitry.

and Eq. ?? respectively indicate.

$$F_{sw_{max}} \rightarrow V_{rset} = 0 \rightarrow R_{total} = \frac{R_{set} * R_1}{R_{set} + R_1} \quad (2.5)$$

$$V_{rset} = V_{cond} * \frac{R_{set}}{R_1 + R_{set}} \quad (2.6)$$

$$V_{cond_{max}} \rightarrow V_{rset_{max}} = 300mV \rightarrow F_{sw_{min}} \approx 0 \quad (2.7)$$

By interpolation of the characteristic's maximum and minimum points Eq. ?? is derived. The  $F_{sw}$  frequency is derived according to the conditioned input voltage ( $V_{cond}$ ). Fig. ?? illustrates the individual nodes' positions according to  $V_{cond}$  output frequency levels as imposed by Eq. ??.

$$F_{sw} = \frac{-F_{sw_{max}}}{V_{cond_{max}}} * V_{cond} + F_{sw_{max}} \quad (2.8)$$

Moreover, Eq. ?? that is derived by Eq. ?? is valid for each WSN node and expresses each node's output frequency level as the function of the VCO input

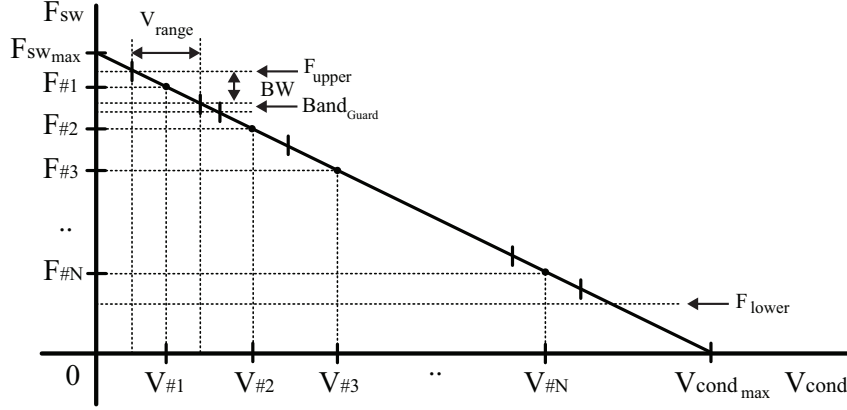


Figure 2.7: The VCO frequency voltage characteristic that indicates the positions of the individual nodes comprising the WSN.

voltage. Fig. ?? illustrates the individual nodes' positions according to  $V_{cond}$  output frequency levels.

$$F_{\#N} = \frac{-F_{sw_{max}}}{V_{cond_{max}}} * V_{\#N} + F_{sw_{max}} \quad (2.9)$$

Eq. ?? is derived by using Eq. ?? and ?? and it provides the output frequency of each WSN node according the  $V_{ref\#N}$  as well as the plant output voltage ( $V_{plant}$ ).

$$F_{\#N} = \frac{-F_{sw_{max}}}{V_{cond_{max}}} * (G * V_{plant} + V_{ref\#N}) + F_{sw_{max}} \quad (2.10)$$

Taking into account the maximum and minimum frequencies of the WSN node, Eq. ?? is derived for calculation the WSN bandwidth that describes the node bandwidth. The value of  $V_{range\#N}$  is given by Eq. ??.

$$BW_{\#N} = F_{H\#N} - F_{L\#N} = \frac{F_{sw_{max}}}{V_{cond_{max}}} * V_{range\#N} \quad (2.11)$$

where,

$$V_{range\#N} = G * (V_{plant_{max}} - V_{plant_{min}}) \quad (2.12)$$

The nodes are allocated inside the available spectrum band by allocating a unique voltage offset for each node. The node's position is set by adjusting the value of  $V_{ref}$  in Eq. ?. The spectrum band is specified by Eq. ?. Due to the

fact that the frequency modulator produces pulses of 50 % duty cycle, the second order harmonics are eliminated. Therefore, the upper bound band's frequency is constrained by the 3<sup>rd</sup> harmonic. Consequently, the  $F_{upper}$  and  $F_{lower}$  upper and lower frequency bounds, respectively, of the backscatter radio band should be set as Eq. ?? indicates.

$$Band = F_{upper} - F_{lower} = \sum_{i=1}^N (BW_{\#i} + Band_{Guard}) \quad (2.13)$$

$$F_{upper} \leq 3 * F_{lower} \quad (2.14)$$

In case that each node occupies the same BW for a given band size the maximum number of nodes that can be allocated are described by Eq. ??.

$$\#Nodes = \frac{F_{upper} - F_{lower}}{BW_{\#N} + Band_{Guard}} \quad (2.15)$$

Figure ?? illustrates the spectrum of the backscattering network. Each node's subcarrier as well as the essential band-guard between each pair of nodes are indicated. Furthermore, the first node's second harmonic is also shown.

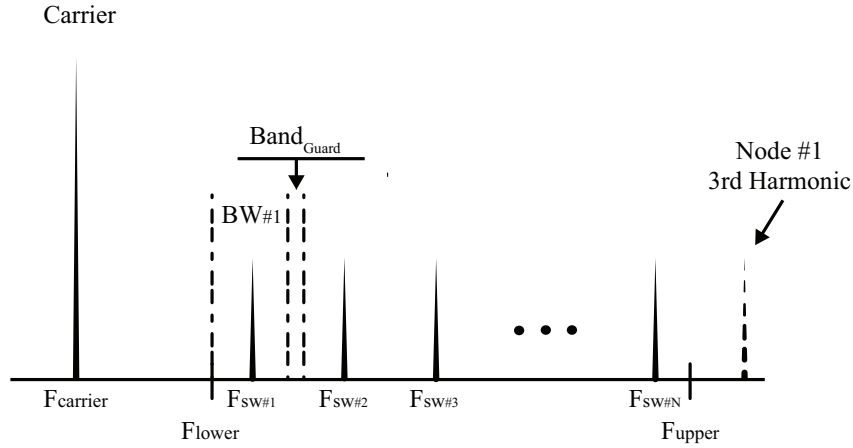


Figure 2.8: Representation of the backscattering sensor network spectrum.

For example, assuming a backscattering band of 100 to 290 kHz and  $V_{range}=25$  mV, then from Eq. ?? and ?? it is derived that the maximum number of nodes that

can be fitted is 95 with a bandwidth of 2 kHz each. Consequently, the number of WSN nodes that can be allocated in a certain backscattering band is upper bounded by the resolution limit of nodes. Thus, the less voltage difference that the node can discriminate, the more nodes can be allocated.

## 2.3 Layout Design

The proposed node was constructed, incorporating the analogue signal-conditioning unit, the subsystem necessary for backscattering the frequency modulated plant signal, as well as the power-supply regulation circuit, on the same PCB board. The PCB layout of the experimental prototype of the proposed WSN node is illustrated in Fig.???. The prototype that was designed is based on a mixed-signal architecture, with separated analogue and digital ground planes, in order to minimize the interference between the voltage controlled oscillator and the analog signal-conditioning unit. The RF front-end layout was designed as the literature describes [?] with the purpose to maximize the efficiency of scatter radio communication.

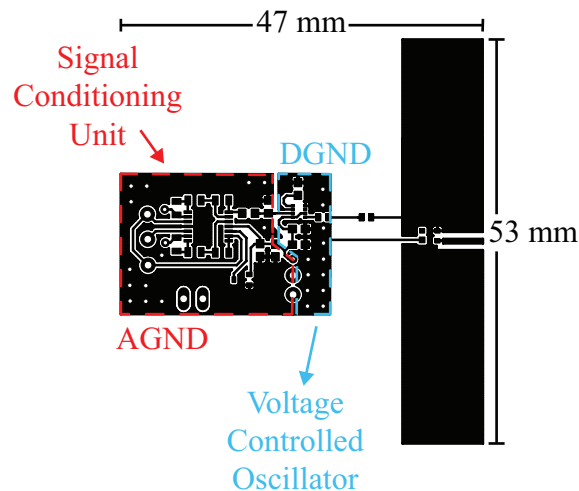


Figure 2.9: The PCB layout of the proposed backscattering plant sensor node.

## Chapter 3

# Energy harvesting from plants

As discussed in Sec. ?? the plants have demonstrated measurable electrical potentials across their stem. This charge can be accumulated and supply electronic modules in a sustainable way. A few works have demonstrated complete ultra-low-voltage systems that are powered solely by plants. Designs of ultra low power level shifters [? ? ] and ultra low voltage boost converter [? ] have been developed with the purpose to condition the power generated by the plants. However, this work demonstrates power-voltage characteristics for first time in the literature, as well as introduces a battery-less ultra low power backscatter sensor node that both interfaces and accumulates the plant electrical signal for monitoring and powering purposes, respectively. Figure ?? illustrates the WSN node's block diagram as well the essential sub-systems for autonomous operation, signal acquisition and scatter radio communication. The system is being designed in a way that the WSN node is operated battery-less by exploiting the plant's electrical power. Initially, the Power Management Unit harvests the low power signal that is generated by the plants. Due to the fact that the available incoming energy is insufficient for the cold-start and the nominal operation of the power converter a duty cycle controlled operation is introduced. When sufficient energy has been accumulated, the PMU supplies the rest of the subsystems that condition the incoming plant signal and modulate the incident carrier accordingly (signal conditioner, voltage controlled oscillator, RF reflective switch).

### 3.1 Plant as a bio-electrical source of energy

Several types of anodes have been deployed in the past literature for the measurement of bio-electrical potentials [? ? ? ]. Zinc and Magnesium alloys are the most popular types of anodes as they offer high open-circuit potential [? ? ].

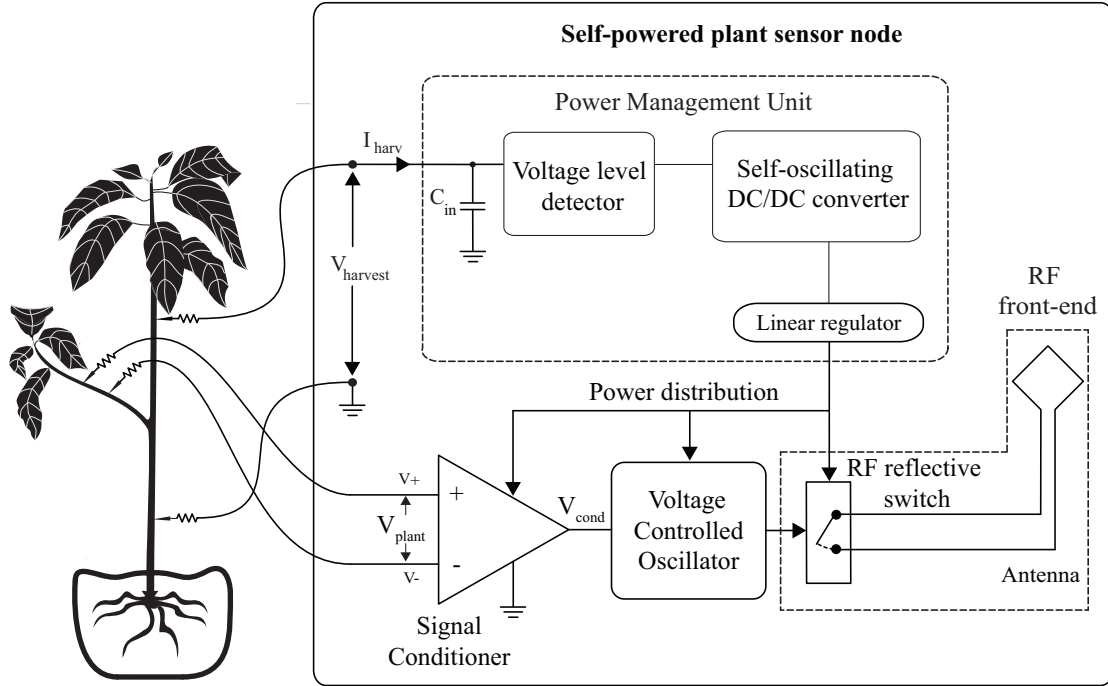


Figure 3.1: A block diagram of the proposed self-powered WSN node.

However, they both show different degradation over time. A few works have employed the plant as bio-electrical sources, however, none of them has yet explored the power-voltage characteristics across the day for different types of anodes. For the purpose of harvesting the bio-potential that is generated by the plants, both anodes were tested in combination with a copper cathode electrode.

Figures ?? and ?? illustrate the power-voltage characteristics of plant avocado across the day for Zinc and Mg alloy electrodes, respectively. In both figures it is noted that the power-voltage characteristics are correlated with the plant's biological procedures which are highly dependent on external stimuli (eg. daylight, temperature, soil moisture). As illustrated, the maximum extracted power varies across the day and obtains its highest value of 370 nW, as well as slightly over 350 nW, at 12:00 with  $860 \text{ W/m}^2$  solar irradiation and  $30.1^\circ\text{C}$  outside temperature in case of Zinc and Mg anodes, respectively. The Maximum Power Points obtain their lowest value of about 170 nW (Zinc alloy anode) and 250 nW (Mg alloy anode) at 20:00 and 22:00 respectively. As clearly depicted, the MPPs vary across the day between the values of 0.4 V and 0.7 V for both cases. Figure ?? illustrates a

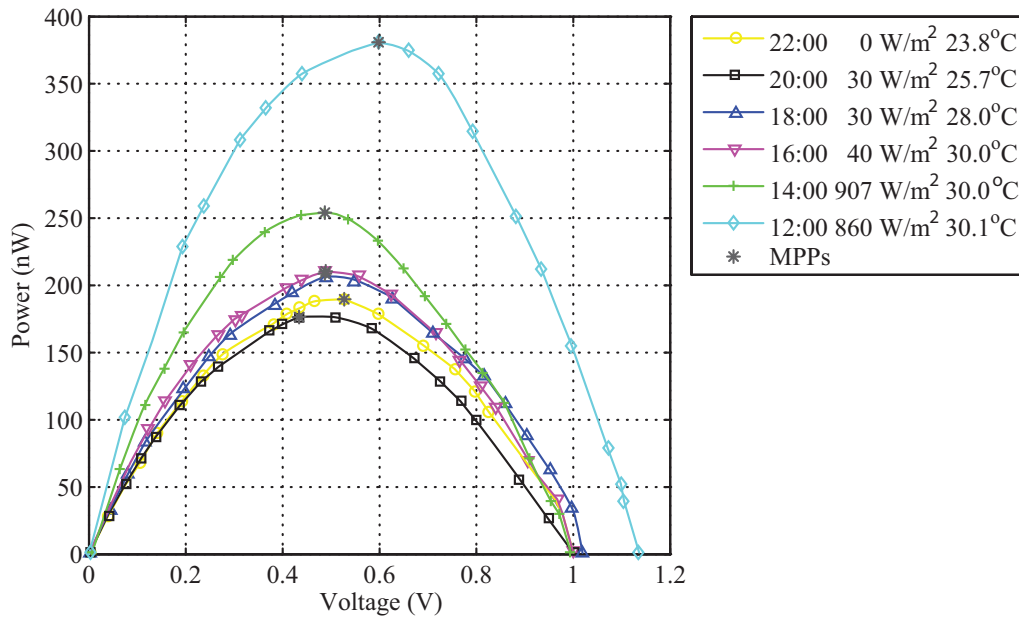


Figure 3.2: Avocado plant power-voltage characteristic for Zinc anode.

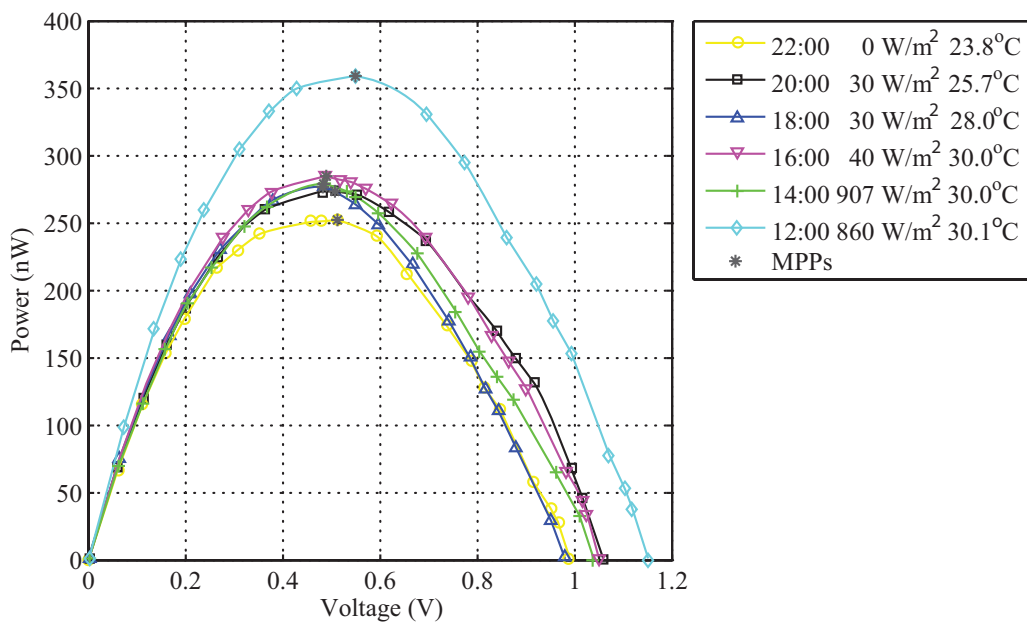


Figure 3.3: Avocado plant power-voltage characteristic for Mg anode.

comparison between the power-voltage characteristics for Mg and Zinc alloy anodes at 12:00 with  $30.1^\circ$  environmental temperature and  $860 \text{ W/m}^2$  solar irradiation.

Both power-voltage characteristics that refer to the employment of Mg and Zinc alloy anodes form concave curves that exhibit a single Maximum Power Point at slightly below and above 0.6 V, respectively. The maximum delivered power for both curves are about 350 nW and slightly below 400 nW, respectively.

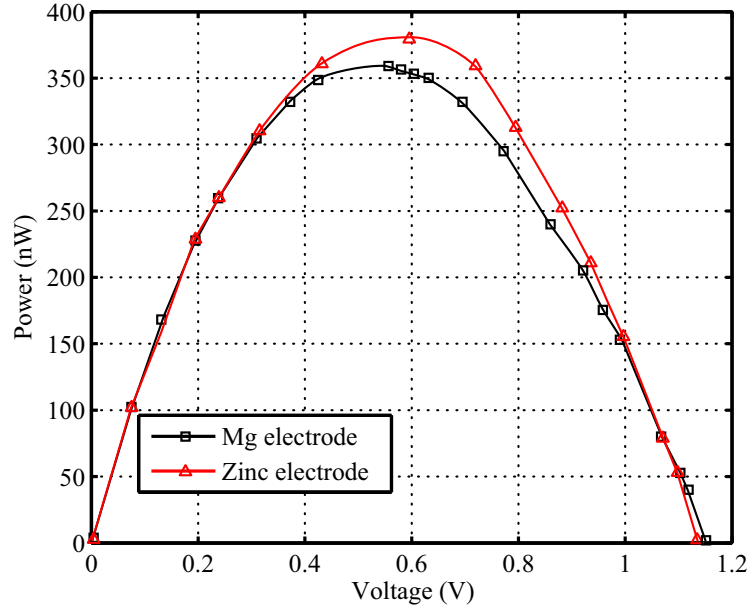


Figure 3.4: Avocado plant's power-voltage characteristic for Mg and Zinc anodes.

Due to the unawareness of the plant electrical equivalent, empirical methods were employed with the purpose to determine the electrodes set-up across the plant's stem. After experiments, it was discovered that as the  $V_{harvest}$  rises, the potential at the  $V_-$  &  $V_+$  measurement points is not affected equally in case that both the measurement and harvesting pairs of electrodes are placed at the same branch. Consequently, the measurement accuracy is disturbed during the system's operation. It was detected experimentally that by placing both the measurement electrodes into another branch, the measurement robustness is reassured. Figure ?? illustrates the optimal electrodes set-up. The measurement Ag pin electrodes of  $V_{plant}$  voltage are attached to the branch, while the anode and cathode electrodes are attached to the stem. The common mode voltage ( $V_{cm}$ ) that is needed for the

operation of the signal conditioning unit is induced by the combination of  $V_-$  input and the anode electrode that is attached into the plant stem and to the system ground reference.

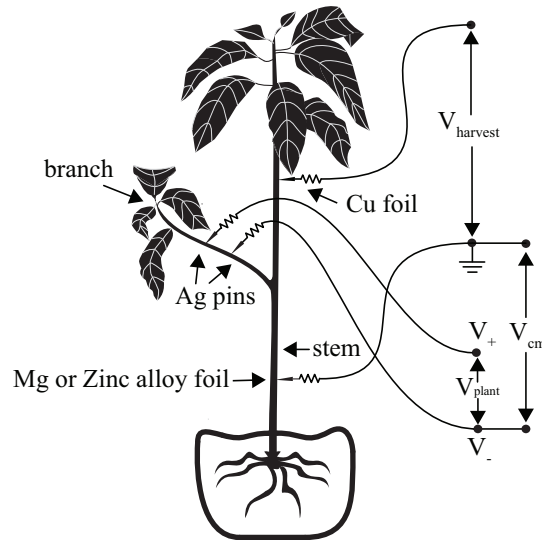


Figure 3.5: The set-up of the measurement and energy harvesting electrodes on the plant.

## 3.2 Power Management Unit

### 3.2.1 Duty-cycle controlled operation

Figure ?? illustrates the PMU architecture. The PMU operates between two voltage levels,  $V_H$  and  $V_L$ , as the voltage detector imposes. During these voltage thresholds the input capacitor  $C_{in}$  is charged and discharged defining the duty cycle operation that the node is on off and on state, respectively. These operational bounds are set to constrain the input capacitor to charge and discharge inside the region that the input power is maximized across the day (0.4-0.7 V), as discussed in Sec. ?. Thus, the power loss that is caused due to the impedance mismatching as the input capacitor charges, is minimized.

The system operates as follows from the cold-start. During the cold-start, the capacitor  $C_{in}$  is charged by accumulating the plant's energy. The voltage detector

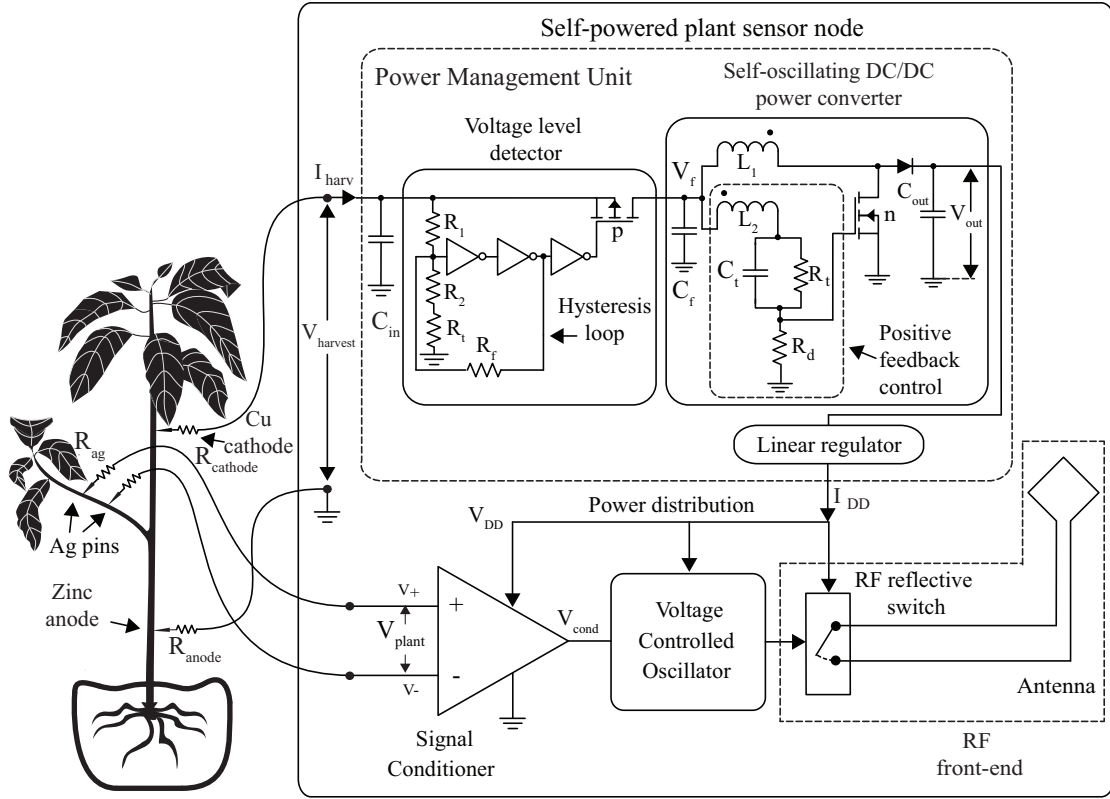


Figure 3.6: A detailed diagram of the proposed self-powered plant sensor node.

constantly monitors the input voltage and keeps the load segregated from the power source. As the capacitor reaches the  $V_H$  voltage level, the voltage detector turns the power converter on and the stored energy flows toward the power converter. The converter steps-up the incoming voltage to a level that the low drop out linear regulator operates and produces the regulated output  $V_{DD}$ . As the  $C_{in}$  capacitor discharges, the voltage input reaches the voltage threshold  $V_L$  and the energy flow toward the power converter seizes. During the operation between of the two input voltage levels ( $V_H$  and  $V_L$ ) the regulated output  $V_{DD}$  powers the RF-front, the signal acquisition unit, as well as the voltage controlled oscillator.

Due to the fact that the harvested current from the plant varies according to the plant's biological procedures, the charging interval ( $t_{off}$ ) cannot be set. Consequently, the power management unit was designed according to the desired operational time ( $t_{on}$ ). The duty cycle  $D$  that the node operates is defined in Eq.

?? and operation time,  $t_{on}$ .

$$D = \frac{t_{on}}{t_{on} + t_{off}} \quad (3.1)$$

Neglecting the internal resistance of the  $C_{in}$  capacitor, the PMU's efficiency during the varying  $V_{harvest}$  input voltage that the duty-cycle-based operation involves for specific  $t_{on}$  operational time and  $V_H$ ,  $V_L$  voltage levels, is calculated using Eq. ??.

$$\eta_{PMU} = \frac{V_{dd} * I_{dd} * t_{on}}{\frac{1}{2} * C_{in} * (V_H^2 - V_L^2)} \quad (3.2)$$

where  $V_{dd}$ ,  $I_{dd}$ ,  $C_{in}$ , refer to the PMU output voltage, PMU output current and the  $C_{in}$  input capacitance, respectively. The numerator refers to the energy spent for powering the load, while, the denominator to the stored energy in input capacitance  $C_{in}$ .

### 3.2.2 Voltage level detector

The voltage level detector as illustrated in Fig. ?? as a part of the PMU unit, constantly monitors the input capacitor's voltage in order to ensure that the power converter voltage input remains between the desired levels. It consists of a hysteresis circuit based on Schmitt trigger architecture that controls the energy flow towards the system. Commercial voltage detector ICs offer triggering voltage levels quite above the 0.6 V threshold that the system operates. Furthermore, most of the implementations of voltage detectors in the literature, comprise complex circuits that are implemented in ICs. The schmitt trigger circuitry that was implemented is a modified version of [? ]. It consist of a scheme of cascaded inverters with positive feedback that ensure the transition between two steady states. The complete circuit is illustrated in Fig. ??.

The voltage divider produces a scaled voltage across the node  $N_1$ . In case that  $V_{N_1}$  is below the threshold voltage  $V_{th}$  of the  $n_1$  Mosfet,  $V_{N_2}$  and  $V_{N_{detect}}$  follow  $V_{harvest}$  while,  $V_{N_3}$  is equal to  $V_{N_1}$  and the  $p_2$ 's gate is pulled up. When  $V_{N_1}$  is above  $V_{th}$ , node  $N_1$  is pulled down and in the same time  $V_{N_3}$  follows  $V_{harvest}$ . Consequently, the  $N_{detect}$  is pulled down and the  $p_2$  Mosfet conducts. The BSH207, as well as the BSH105, p-channel and n-channel Mosfets, respectively, were employed

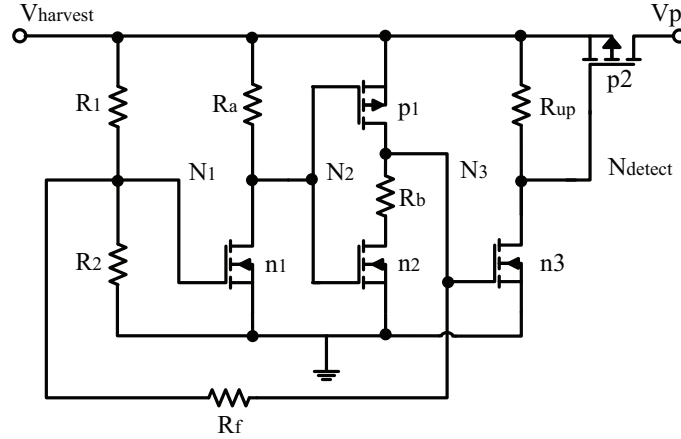


Figure 3.7: Topology of the voltage detector circuit.

to implement the voltage level detector since they have an ultra low threshold voltage  $V_{th}$ .

In contrast to the implementation of the voltage detector circuitry in [? ], in this work the p-Mos of the inverter before the Mosfet in series with the load, was substituted by a pull-up resistor due to the fact that the voltage threshold of the p-Mos transistor hampers the proper function of the schmitt trigger under low voltage input. The circuit's states are alternating whenever the value of the  $C_{sto}$  capacitor voltage,  $V_{sto}$ , crosses the two hysteresis thresholds  $V_H$  and  $V_L$ . Equation ?? and ?? describe the  $V_H$  and  $V_L$  hysteresis levels.

$$V_H = \left(1 + \frac{R_1}{R_H}\right) * V_{th} \quad (3.3)$$

$$V_L = \left(1 + \frac{R_L}{R_2}\right) * V_{th} \quad (3.4)$$

where,

$$R_H \simeq \frac{R_2 * R_f}{R_2 + R_f} \quad (3.5)$$

$$R_L \simeq \frac{R_1 * R_f}{R_1 + R_f} \quad (3.6)$$

Figure ??(a) illustrates the operation of signal  $V_{Ndetect}$  according to the value of

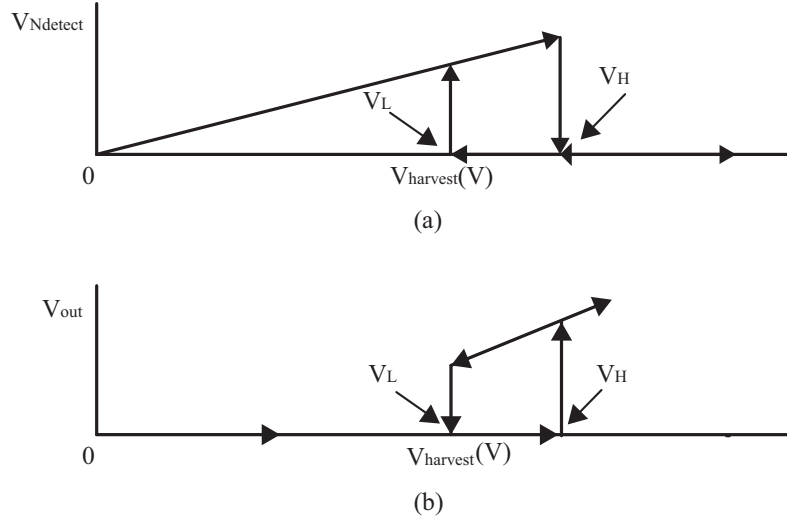


Figure 3.8: Topology of the proposed circuit.

the  $V_{harvest}$  input. As  $V_{harvest}$  increases, the voltage at the  $N_{detect}$  node follows  $V_{harvest}$  input till the  $V_H$  voltage threshold is reached, afterwards,  $N_{detect}$  signal is pulled down. When the  $V_{harvest}$  input starts to degrade the  $V_{N_{detect}}$  signal remains pulled down until the  $V_{harvest}$  input reaches the  $V_L$  threshold. Figure ??(b) depicts the voltage detector's output as the  $V_{harvest}$  fluctuates. The output  $V_{out}$  remains close to zero as the  $V_{harvest}$  augments. When the voltage threshold  $V_H$  is reached, the value of  $V_{out}$  follows  $V_{harvest}$ . As  $V_{harvest}$  is diminishing and crosses the  $V_L$  threshold, the voltage detector changes state of operation and the  $V_{out}$  drops to zero.

The voltage detector was designed to interface the ultra low power signals that are generated by the plant. Apart from the resistors  $R_f$ ,  $R_1$  and  $R_2$  that were set such that to define the  $V_H$  and  $V_L$  voltage threshold, the values of  $R_a$ ,  $R_b$  and  $R_{up}$  were set in a way the voltage detector effectively harvests the low power signals that are generated by the plant. The overall value of the input resistance of the voltage detector, during the  $t_{off}$  charging interval, should be large enough to ensure that the quiescent current that flows towards the voltage detector is many times smaller than the harvested current that charge the input capacitance  $C_{in}$ . As the voltage input augments towards the  $V_H$  threshold, the positive feedback hinders the  $n1$  Mosfet to open. Nevertheless, the drain-source current that flows

from the n1 towards ground slightly increases. In case that the  $R_a$  is not set such that to prevent this current flow or the harvested current is inadequate, the charging process of  $C_{in}$  capacitance halts as the input voltage does not reach the  $V_H$  threshold. Furthermore,  $R_a$  and  $R_{up}$ , that serve as pull-up resistors, should be set such that to effectively bias the corresponding n-Mosfets as well as to maintain the power consumption to ultra low levels. The  $R_b$  resistor diminishes the high instantaneous current that flows towards the source of transistor n2 during the transition between the two states.

For seamless operation of the voltage detector it should be ensured that the voltage levels remains unaffected under every environmental condition. In this context, by sensitivity analysis of Eq. ?? and ?? it is proved that every resistance that is included into the design is equally affected by temperature changes, it thus does not affect the voltage thresholds. However, the Mosfet transistors that are used to implement the voltage detector exhibit a sensitivity of threshold with ambient temperature. Consequently, the voltage detector's voltage thresholds are affected accordingly. As the temperature increases, the Mosfets  $V_{th}$  threshold reduces. Thus, from Eq. ?? and ?? it can be inferred that the sensitivity of the voltage detector's upper and lower thresholds with temperature can be compensated by integrating a Negative Temperature Coefficient (NTC) thermistor in series with the voltage divider resistance  $R_2$ . In such a case, the new value ( $R'_2$ ) of the  $R_2$  resistance is  $R'_2 = R_2 + R_t$ , where  $R_t$  is thermistor resistance. However, as the change of the value of  $R_t$  does not affect equally both the  $V_H$  and  $V_L$  thresholds of the voltage detector, a perfect compensation cannot be achieved.

### 3.2.3 Self-Oscillating DC-DC Power Converter

A common issue of the power converter's operation constitute the cold-start under low power input as well as the powering of the converter's control circuit under cold-start conditions. In this state the system energy storage, that supplies among other sub-systems the control circuit, suffers complete drainage of energy. Consequently the power conditioning unit is not able to operate by extracting energy from the source. Among the solutions that have been proposed in the literature, the simplest solution remains the self-oscillating converter, which does not deploy

complex control circuitry. Several designs have been proposed that utilize Colpitts oscillator structure combined with power converter [? ? ? ? ?]. These structures can be viewed as positive feedback systems that produce and sustain the oscillations by feeding back a fraction of the output signal as well as use an amplifier to gain the signal. The remnant fraction of energy is accumulated after the output  $V_{out}$  is rectified and produces the stepped-up output of the converter. Fig. ?? illustrates the positive feedback control scheme of a self-oscillating converter for input control signal  $V_{con}$ . The  $f(s)$  component represents the control and frequency selection circuit. The  $A(s)$  component consists of the amplifier and its biasing circuitry that is essential for the amplification of the produced signal, while, component  $B(s)$  contributes to the rectification and accumulation of the conditioned signal.

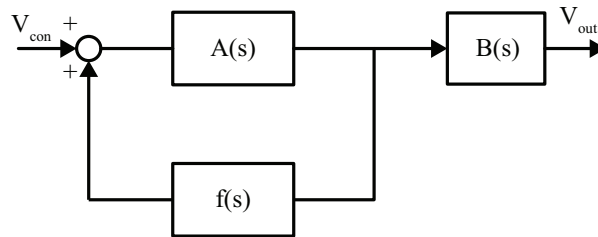


Figure 3.9: Self-oscillating DC-DC converter block diagram.

These architectures employ either common boost converter schemes [? ], [? ] (top.1), [? ] or flyback converter structure [? ] (top. 2& 3), [? ?]. The flyback architectures utilize high turns ratio transformers that offer a high step-up voltage, however they lack in conversion efficiency in contrast to the conventional boost converter architectures. The location of the maximum power points of the plant's characteristic across the day, as shown in Sec. ??, impose that the power converter should be able to operate close to the maximum power point that range from 0.4 V to 0.7 V. In the same time, it should be able to step-up the input voltage at 1.6 V so that the subsystems of the WSN node are able to operate. Considering these constraints, the DC-DC converter of [? ] suits to the application under study as it provides a high step-up ratio and in the same time constitutes a boost converter topology. The corresponding circuit is depicted in Fig. ?. Complementary to the power converter a voltage reference IC is employed in order

to regulate the output voltage to the needed voltage level (i.e. 1.6V). During the

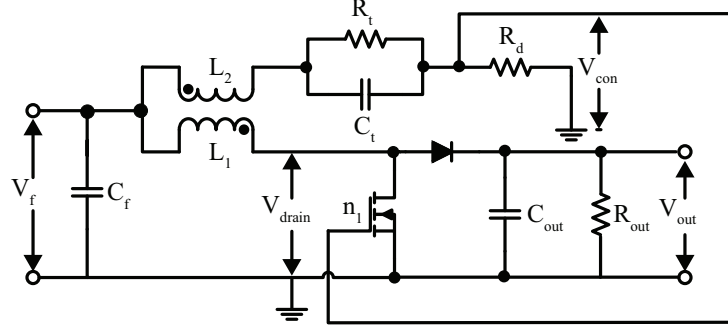


Figure 3.10: The circuit of DC-DC converter employed in the proposed WSN node.

cold-start, the Mosfet  $n_1$  is in the off state. As the supply voltage raises, the voltage at the gate of transistor  $n_1$  and the current of the inductor  $L_1$  raises as well. Meanwhile, a voltage is induced in the secondary winding, which charges the oscillating tank comprised of  $R_t$  and  $C_t$ . As transistor  $n_1$  completely conducts, then current of  $L_1$  remains constant. Consequently, the voltage that is induced in  $L_2$  drops to zero and capacitor  $C_t$  starts to discharges into  $C_f$ . As the capacitor discharges, the voltage at the gate of the transistor  $n_1$  starts to decrease. When it is completely turned-off, the available energy that is stored in the primary winding flows towards the rectifier and the output capacitor. As the current of the primary winding decreases a voltage is induced into the secondary winding and therefore the capacitor  $C_t$  is charged. The output voltage ripple is wiped out by capacitor  $C_{out}$ .

The simulated waveforms  $V_{con}$ ,  $V_{drain}$ ,  $V_{out}$  and  $V_{in}$  signals are shown in Fig. ???. The simulation was performed with the following values of the components:  $R_t = 330 \Omega$ ,  $C_t = 6.8 nF$ ,  $L_1 = 12 uH$ ,  $L_2 = 12 uH$ ,  $C_f = 440 uF$ ,  $C_{out} = 3 uF$ ,  $R_d = 15 M\Omega$  and an ohmic load of  $305 k\Omega$ . The  $L_1$  and  $L_2$  values of the transformer affect the oscillating frequency, as well as the current that is injected into the load. These values, accompanied with the values  $C_t$  and  $R_t$  of the oscillation tank were selected with the purpose to obtain an oscillation frequency of 1.66 MHz that enables the minimization of the losses as well as maximize the transformer's coupling coefficient. Furthermore an output voltage of over 1.6 V is produced at the lowest operational input voltage that enables the seamless supply of the load

after the voltage conversion to 1.6 V voltage level by the voltage regulator.

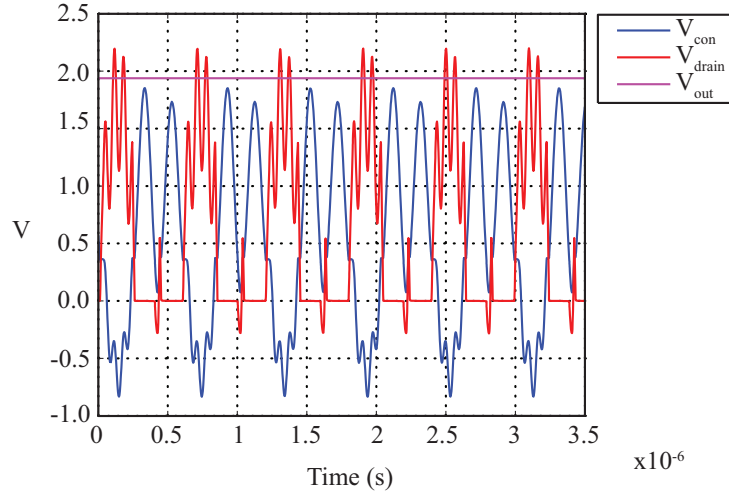


Figure 3.11: Simulated waveforms of the DC-DC converter signals.

### 3.3 Layout Design

The proposed WSN node is designed in a way that minimizes the interference of the modulated output signal to the analogue unit. In the same time, the regulated output that supplies the signal condition unit, the voltage-controlled oscillator and RF front-end should be eradicated from noise that flows out from the switching DC-DC power converter converter. Figures ?? and ?? illustrate the top and bottom layer, respectively of the node PCB layout that was designed to fulfil the aforementioned specifications. The analogue ground (AGND), the digital ground (DGND) and the RF front-end that correspond to the signal conditioning unit, the voltage-controlled oscillator and the RF switch, respectively, are connected in a star configuration with the ground plane of the power management unit (GND).

The planar transformer is located close to the power management unit and in the same time remains in a distance from the analogue ground with the purpose of minimizing the interference. With an aim to maximize the coupling coefficient, the windings are nested each other, in the same layer.

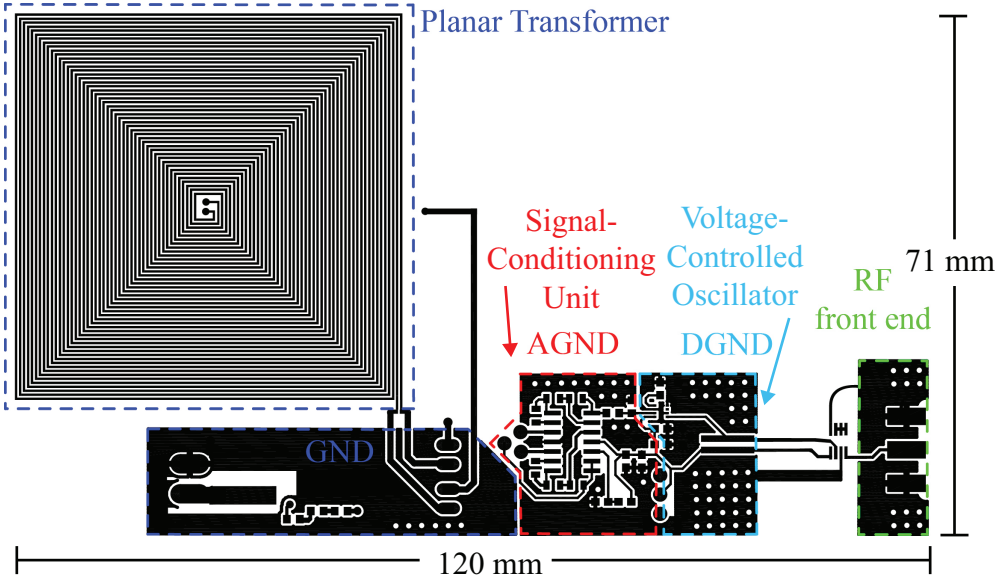


Figure 3.12: Top layer of the self-powered scatter radio node PCB.

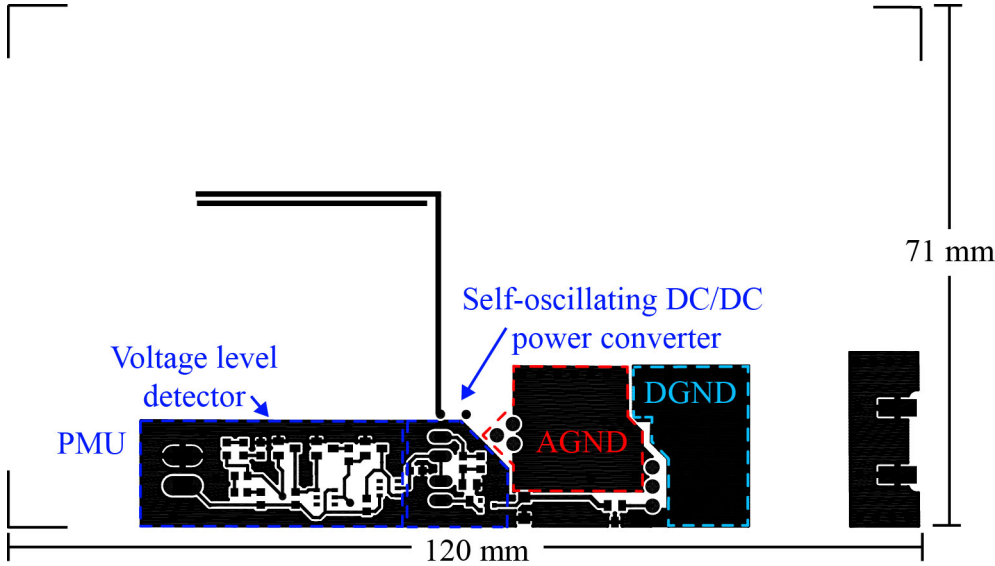


Figure 3.13: Bottom layer of the proposed self-powered scatter radio node PCB.

# Chapter 4

## Receiver Design

The Frequency Division Multiple Access, Medium Access Control protocol is deployed to achieve seamless communication among the WSN nodes. As described in Sec. ?? the receiver should be able discriminate each node's subcarrier. Furthermore, in the case of the self-powered WSN node, the receiver should be able to adapt to the duty-cycle-based operation of the node. The receiver software that handles the FDMA protocol was implemented according to [? ]. Complementary to this work, an energy based signal detection feature was implemented that handle the duty-cycle-controlled operation of the WSN node.

### 4.1 FDMA receiver

For the implementation of the receiver, a homodyne Universal Software Radio Peripheral architecture has been employed exploiting the GNU radio platform. Initially, the signal is received and demodulated by returning it to the baseband. After the signal is digitized, it is retrieved in packets according to the rate that it is read and processed by the receiver software. Due to the frequency offset that is appeared between the receiver and the emitter a Carrier Frequency Offset (CFO) compensation is needed. During the CFO procedure, the emitter carrier is estimated and is set at the zero position. Consequently, the frequency that the sub-carrier appears is consistent with the actual modulation frequency of the WSN node. Afterwards, band-pass filtering is applied to the allocated band of each node. Each node frequency is calculated by Eq. ??.

$$\hat{F} = \arg \max_{F \in [F_L, F_U]} |X(F)|^2 \quad (4.1)$$

where  $X(F)$  is the spectrum band of each node and  $F_L$  and  $F_H$  is the upper and low bounds of frequency for each node.

Sliding histogram filtering was utilized to filter out the noisy artifacts of the receiving backscatter signal, as was implemented in [? ]. Specifically, each measurement arises from the outcome of the sliding histogram filtering process of one hundred received packets of 0.1s duration each. Consequently, the noise that occurred during low SNR communication is filtered out. The filter was configured to comprise 400 bins and a sliding window of 40 bins.

### 4.1.1 Duty Cycle Handler

The duty cycle handler is designed to detect the incoming packets as the self-powered node operates. Figure ?? illustrates the reader's process. Initially, the sensor's band noise floor is estimated by calculating the energy spectral density of the allocated band when the node does not transmit. The receiver retrieves packets continuously until a predefined energy density is reached at the desired spectral band that is above the energy density of the noise floor plus a predefined safety threshold. The duty cycle operation imposes that the energy of a signal is transmitted for a certain time period,  $t_{on}$ , within a total operating period  $T_{op}$ . Eq. ?? expresses the transmitted signal spectral energy for a  $t_{on}$  time span.

$$E_f = \int_0^{t_{on}} |f(t)|^2 dt \quad (4.2)$$

It is clearly denoted that the signal's spectral energy is maximized as the value of  $t_{on}$  is increased, thus, the Signal Noise Ratio is increased accordingly.

Initially the magnitude of the noise floor is calculated. During the execution loop of the reader as illustrated in ??, packets are retrieved constantly and CFO compensation is performed to the retrieved packet. Moreover, Fast Fourier-Transform and Band-Pass filtering are applied around the node frequency bandwidth that it has been set. When the desired amplitude is detected the receiver breaks the loop, reads the environmental temperature and estimates the plant voltage. The node sub-carrier frequency is calculated using Eq. ??.

The node duty cycle operation imposes that the receiver should detect the in-

---

coming signal whenever it appears, without requiring knowledge of the exact duty cycle. Thus, the receiver should be operate as such that no packet is missed. Due to the fact that the receiver processing time increases as the sampling frequency augments, the sampling rate should be as close to the Nyquist's frequency of the upper frequency of the allocated WSN spectrum band. It was detected experimentally that for a transmission time of about 100 ms, the optimal packet length is about 100 ms. During the operation of the WSN node several packets are retrieved by the receiver that contain the node sub-carrier. Among the detected packets, the node's sub-carrier frequency is calculated by the packet that the sub-carrier energy density maximizes thus, the errors are minimized.

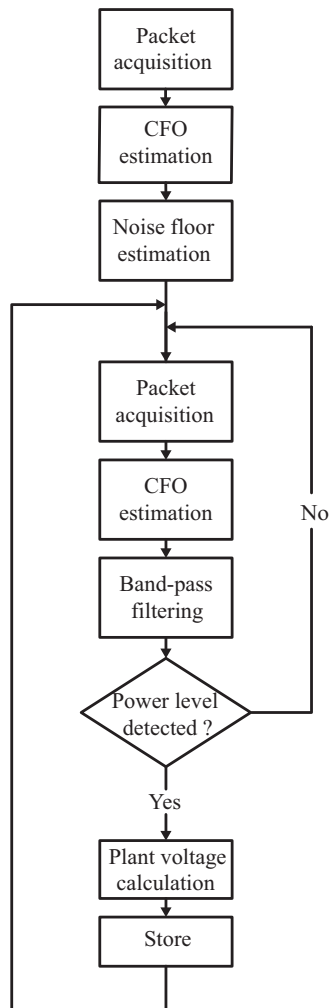


Figure 4.1: Flow-chart of the receiver software.

# Chapter 5

## Experimental Results

### 5.1 Self-Powered Plant Signal Acquisition Node Setup

The topology of the proposed WSN that was followed during the experimentation process, is illustrated in Fig ???. In terms of demonstrating the harvesting operation two nodes were fabricated. One of the prototyped nodes accompanied with IP65 rated casing and monopole antenna is illustrated in Photograph ?? in the Appendix. The harvesting and measurement electrodes were set as Photograph ?? illustrates. The inlet illustrates the anode that was attached to the plant. The frequency bands occupied by these two WSN nodes, for the entire range of the plant signal voltage levels, were set at 868.016-868.021 MHz and 868.023-868.030 MHz, respectively, in order to ensure that the bandwidths occupied by the individual WSN nodes do not overlap. Figure ?? illustrates the carrier and subcarriers of the scatter radio operation for input voltage of -600 mV and +600 mV for each node.

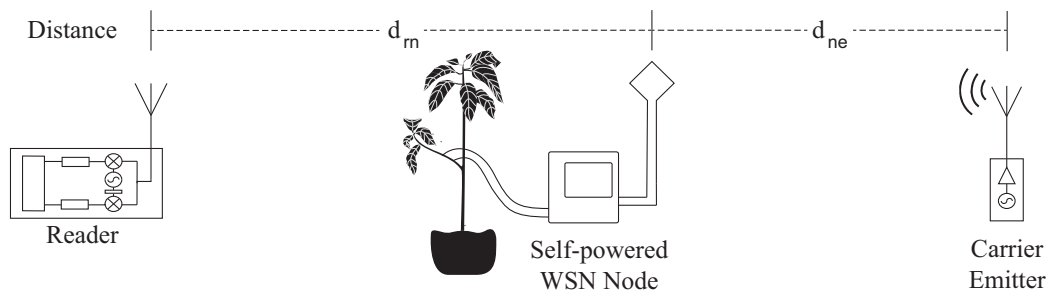


Figure 5.1: The topology of the proposed WSN during the experimentation process.

The self-oscillating DC-DC converter was implemented to step-up the input

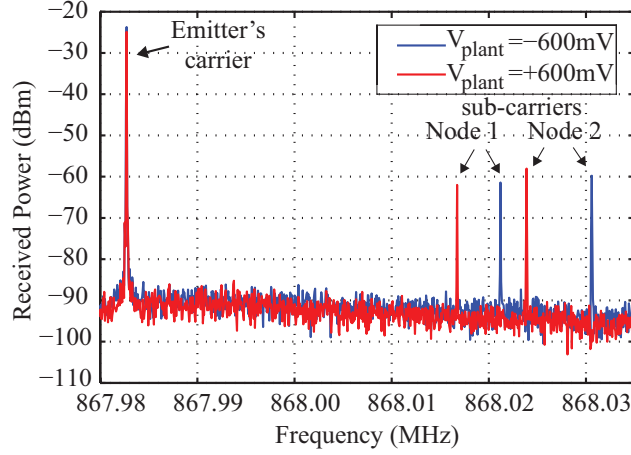


Figure 5.2: The frequency spectrum for two operating nodes, at alternative input voltage levels.

voltage of 0.58 V to 1.60 V. The oscillator tank and the coupled inductor were set as follows:  $R_t = 330 \Omega$ ,  $C_t = 6.8 \text{ nF}$ ,  $L_1 = 13 \text{ uH}$ ,  $L_2 = 12.3 \text{ uH}$  and a coupling coefficient of 0.96. Regarding the  $R_d$  resistance, the Mosfet BSH105 input resistance, that is on order of  $M\Omega$ , is adequate to induce the control signal ( $V_{con}$ ) into the Mosfet gate, thus,  $R_d = \infty$ . The switching frequency of the DC-DC converter has been measured to 1.15 MHz. The discrepancy between the measured and simulated frequency major is caused due to the non-ideal characteristics of the planar transformer and the components that was implemented. The ultra low drop-out HSMS-285B diode was utilized, as well as the low voltage threshold Mosfet BSH105. The coupled inductors were implemented as a planar PCB design with an air gap that has zero fero-magnetic core losses. Furthermore, the voltage reference that was employed is the MAX6018 that consumes about  $5 \text{ uA}$  at  $1.8 \text{ V}$  input voltage. Figures ??, ?? and ?? illustrate the  $V_{out}$ ,  $V_f$  and  $V_{drain}$  signals, respectively in correspondence with the  $V_{con}$  signal during the experimental operation of the DC-DC power converter at  $V_{harvest} = 553 \text{ mV}$ . The power conversion efficiency of the PMU for different  $V_{harvest}$  input is indicated in Table ?. From Table ? it

can be inferred that as the  $V_{harvest}$  augments the efficiency decreases reaching 0.64 % at  $V_{harvest} = 0.826$  V. Figure ?? illustrates the operational points of the self-oscillating DC-DC converter for various loads and different voltage ( $V_{harvest}$ ) input levels. These points ensure that the necessary oscillation for the operation of the DC-DC power converter has occurred. The experimentally measured conversion efficiency of these operational points is depicted in Fig. ??.

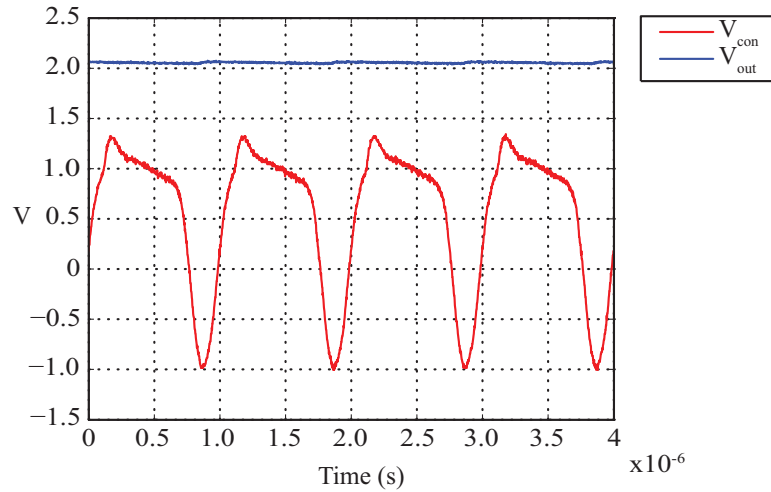


Figure 5.3: The experimentally measured waveforms of  $V_{con}$  and  $V_{out}$ .

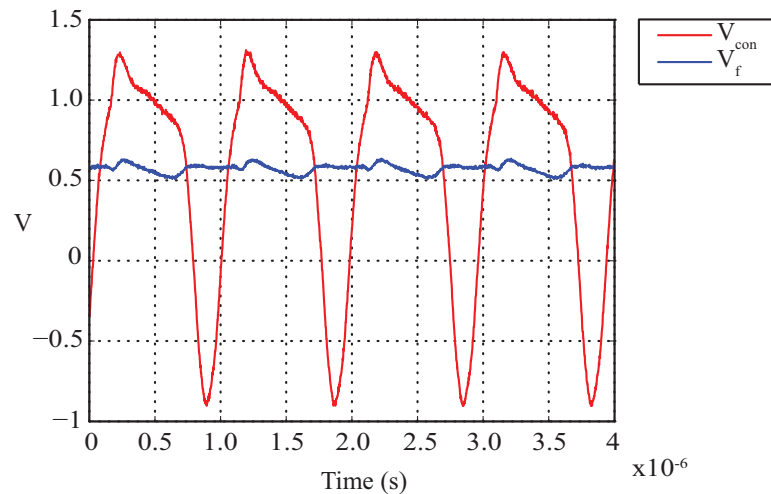


Figure 5.4: The experimentally measured waveforms of  $V_{con}$  and  $V_f$ .

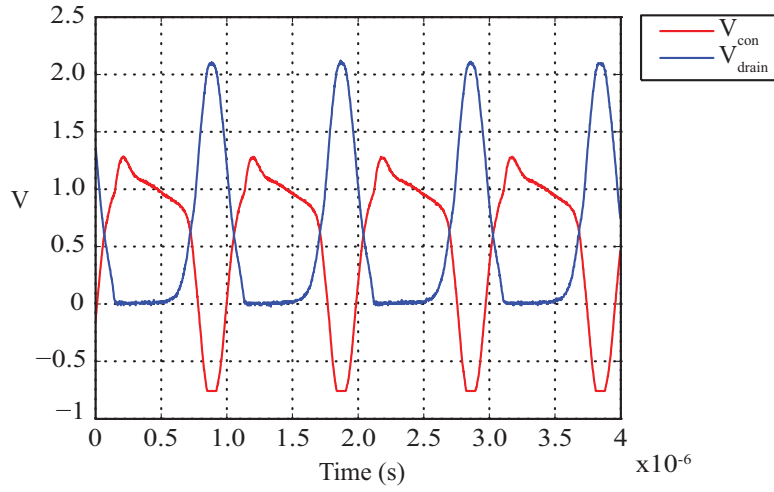


Figure 5.5: The experimentally measured waveforms of  $V_{con}$  and  $V_{drain}$ .

$V_{harvest}(V)$	0.826	0.784	0.647
$\eta_{PMU} \%$	0.64	0.80	2.1

Table 5.1: Efficiency of the PMU for different input voltage levels ( $V_{harvest}$ ).

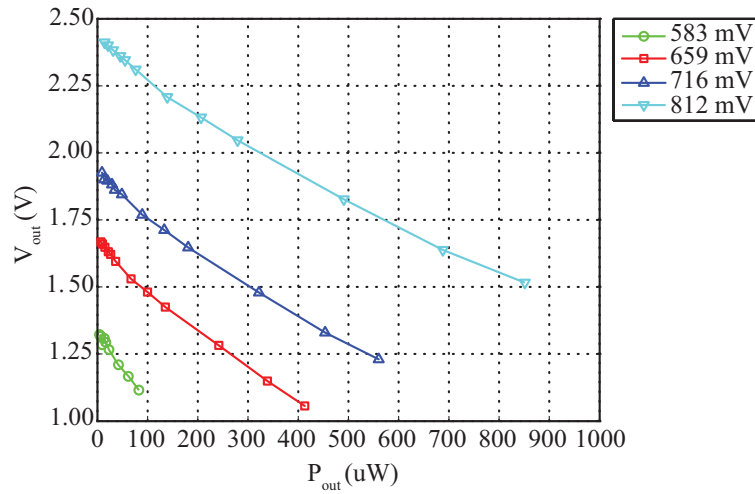


Figure 5.6: Experimentally measured output voltage ( $V_{out}$ ) for various loads of DC/DC power converter and different voltage levels of the  $V_f$  input.

Despite the fact that a perfect compensation cannot be achieved by setting the  $R_1$ ,  $R_2$ ,  $R_t$  values, the temperature compensation range can be set to satisfactory levels adapted to the ambient temperature conditions on any target installation

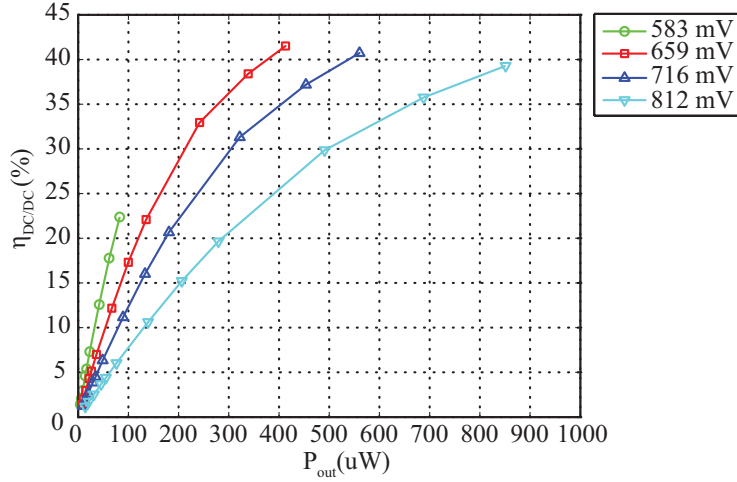


Figure 5.7: The experimentally measured conversion efficiency of the DC-DC power converter for various loads and different voltage levels of the  $V_f$  input.

$C_{in}$ ( $\mu F$ )	2350	2820	3350	3820	4350
$T_{on}$ (ms)	176	194	247	266	274

Table 5.2: The experimentally measured transmission times of the self-powered node for various values of the input capacitor,  $C_{in}$ .

site by appropriately matching the values of  $R_t$ ,  $R_1$  and  $R_2$ . As an example, in the experimental prototype circuit of the proposed WSN node which was developed, using  $R_t = 5.6 M\Omega$ ,  $R_1 = 5.8 M\Omega$  and  $R_2 = 3.3 M\Omega$  resulted in a variation of  $V_H$  and  $V_L$  in the ranges of 703 - 635 mV and 553 - 544 mV, respectively, for a 2.0 - 29.0  $^{\circ}C$  ambient temperature change. The  $t_{on}$  operating time interval, for ambient temperature values in the range of 2.0 - 29.0  $^{\circ}C$ , varies between 236 - 153 ms for  $C_{in} = 2350 \mu F$ . The experimentally measured transmission times of the proposed WSN node for various values of the input capacitor,  $C_{in}$ , are presented in Table ??.

Figure ?? illustrates the cold-start procedure as well as the charge and discharge cycles of the power management unit, while it harvests energy from the plant. As clearly denoted, after the cold-start procedure that spans for about 1130 sec ( $t_{cold-start}$ ), the input starts to fluctuate between the  $V_H$  and  $V_L$  voltage thresholds. Figure ?? illustrates the operation of the power converter according to the PMU input during the  $t_{on}$  interval of transmission. As depicted, the system operates from

a cold-start. The voltage detector operates until the voltage input drops to  $V_L$ . During that interval the power converter instantly starts and produces an output ripple. Figure ?? depicts the operation of the voltage-controlled oscillator during the  $t_{on}$  operation time. A typical value of duty cycle  $D$ , as calculated from the  $t_{off}$  and  $t_{on}$  time intervals (as denoted in Fig. ?? and Fig. ??), is  $3.80 * 10^{-4}$  with  $C_{in} = 2350 \mu F$ . It should be noted that the duration of the cold start time interval as well as  $t_{off}$  charging time, depend on the amount of power extracted from the plant. The PMU efficiency during the  $t_{on}$  operational time that is indicated in Fig.?? is 1.3 % as calculated from Eq. ??.

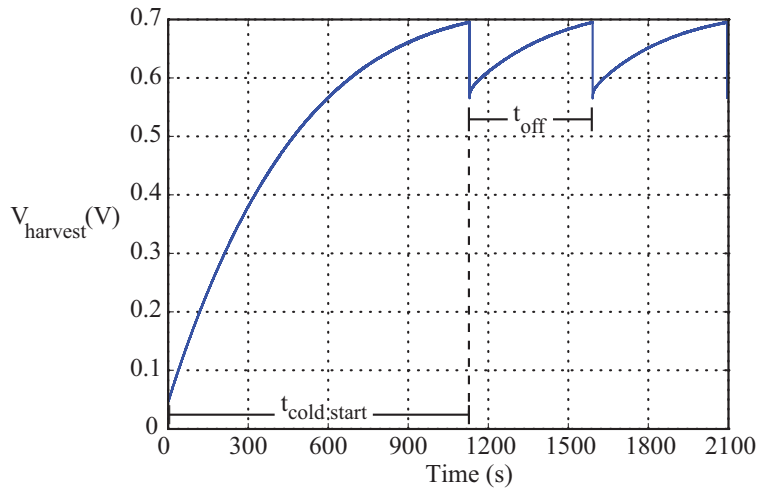


Figure 5.8: Duty cycle operation of the PMU unit.

The node's frequency-voltage sensitivity measured by the reader is about  $56.5 \text{ Hz}/10 \text{ mV}$ . Two alternative configurations of the bistatic topology were investigated, where the distances between the Reader and the WSN node (i.e. distance  $d_{ne}$  in Fig. ??) were set at  $14.6 \text{ m}$  and  $19.3 \text{ m}$ , respectively, while the reader-to-emitter distances (i.e. distance  $d_{rn}$  in Fig. ??) were equal to  $27.9 \text{ m}$  and  $35.7 \text{ m}$ , respectively. The resulting values of the mean Signal to Noise Ratio (SNR), as well as the Root Mean Square (RMS) and Mean Absolute Error (MAE) of 100 consecutive measurements are presented in Table ?. By applying appropriate signal-processing schemes in the Reader software, as implemented in [? ], an operational distance  $d_{rn}$  of about  $96 \text{ m}$ , as well as a distance  $d_{ne}$  equal to  $40 \text{ m}$  can be achieved that results in lower received SNR, with the same (100 ms) received

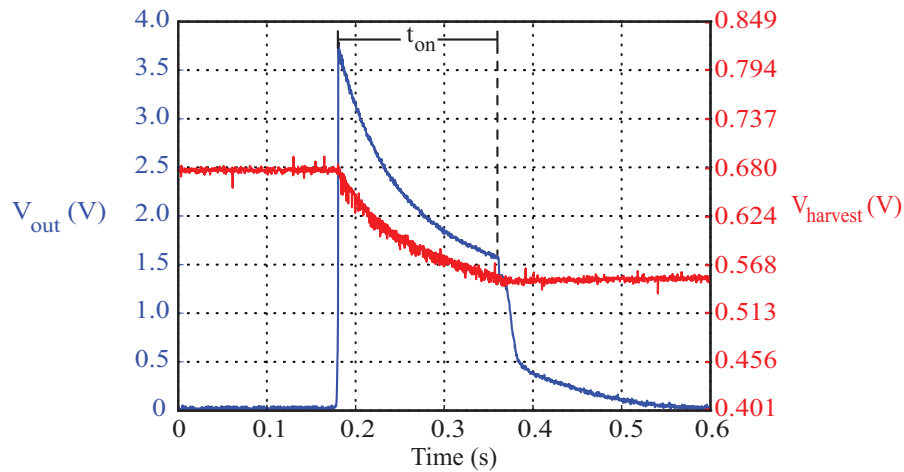


Figure 5.9: The input and output voltage waveforms of the DC-DC converter.

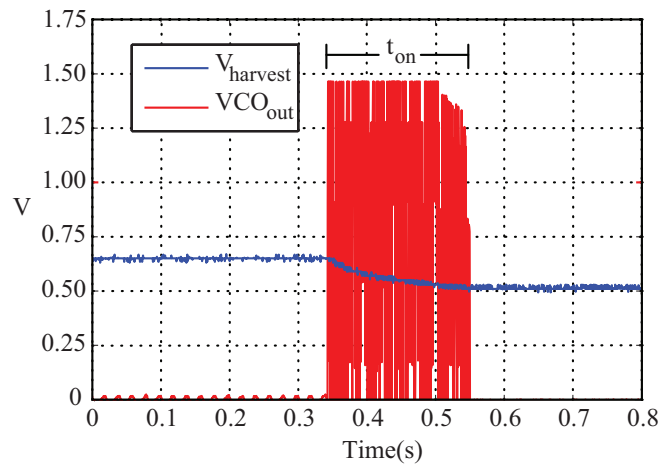


Figure 5.10: Output of VCO ( $VCO_{out}$  as defined in Fig. ??) during the  $t_{on}$  interval of operation and the corresponding value of the  $V_{harvest}$  input voltage.

packet duration.

## 5.2 Battery-powered Plant Signal Acquisition Network Setup

For the purpose to demonstrate the networking capabilities of the proposed design, eight battery powered nodes were also fabricated and calibrated. One of the

Topology Configuration	SNR (dB)	Error	
		RMS (mV)	MAE (mV)
1	25.57	16.04	14.58
2	23.80	25.40	25.35

Table 5.3: Signal to Noise Ratio, Mean Absolute Error and Root Mean Square Error for two alternative bistatic configurations.

prototypes is depicted in Photograph ???. Photograph ?? illustrates 4 of the implemented nodes during the plant signal acquisition process accompanied with their corresponding Avocado plants, the emitter, the reader and the environmental sensors of humidity, temperature and solar irradiation. The Ag pin electrodes were set as photograph ?? indicates. All the nodes were implemented as described in Sec. ??. The  $F_{upper}$  and  $F_{lower}$  bounds were set at  $145\text{ kHz}$  and  $290\text{ kHz}$  respectively. The sensitivity of the nodes is equal to  $40\text{ Hz}/5\text{ mV}$ . The spectrum band was set at  $145\text{ kHz}$ . Furthermore, each node was set at a bandwidth of  $4.5\text{ kHz}$ . The guard-band between each pair of nodes was set to  $500\text{ Hz}$ . The maximum number of nodes that are able to be allocated in the prototyped network are 32 nodes. However, the capacity of the network can be augmented to 42 nodes by setting the  $F_{lower}$  frequency bound to  $96\text{ kHz}$  that is the minimum allowable lower bound due to the  $3^{rd}$  harmonics. Each node was designed to operate within an input voltage range  $-250\text{ mV}$  to  $+250\text{ mV}$ . Custom bow-tie antennas as shown in Photograph ?? were attached to the prototype nodes with coaxial cable with the purpose to cover the needs of the scatter radio communication. In case of the signal emitter and receiver, monopole antennas were used for omnidirectional coverage.

### 5.3 Calibration

After the estimation of each node's frequency as described in Sec. ?? the corresponding plant voltage is calculated by a polynomial equation that is extracted by a process of calibration. The prototyped nodes exhibit a non-linear response regarding the input-output characteristic, as well as a temperature sensitivity that is correlated with the circuit components tolerance. In order to desensitize this

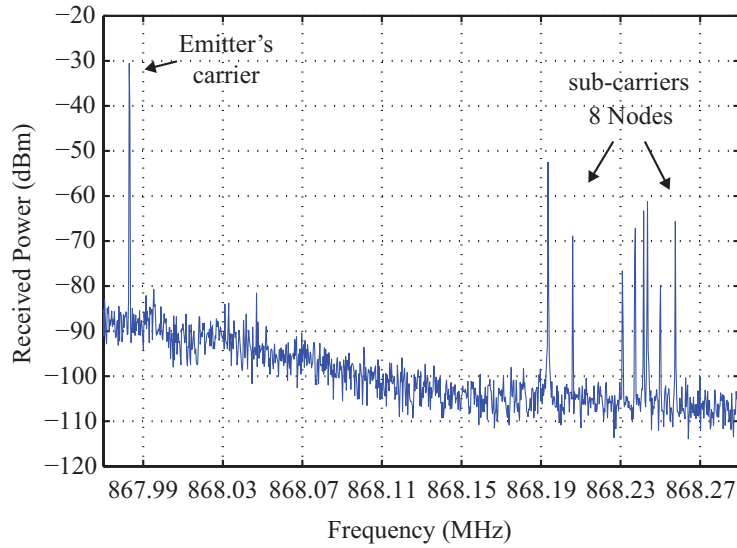


Figure 5.11: Frequency spectrum of eight operating nodes during the wireless signal acquisition process.

non-ideal response, the node was calibrated with a variable differential signal as input, across different environmental temperature conditions.

The process was conducted end-to-end including the communication link and the reader process. A floating triangular signal generator was connected to the  $V_{plant}$  input. Due to the fact that a common-mode voltage should be set for the operation of the signal acquisition unit, the  $V_-$  pin of the generator was connected both to the plant and the corresponding signal-conditioner input. In case of the self-powered node, with the purpose to emulate the source of energy, a DC power supply powers the node as it is connected to the Power Management Unit through the  $V_{in}$  pin. Figure ?? illustrates the calibration setup of the self-powered node as it was realized. The DC power supply as well as the WSN node were grounded on the plant.

The least squares fitting was opted to provide a polynomial equation that expresses the sensed voltage according to temperature and received frequency of the calibration data. Figure ?? illustrates the fitting curve that is described by the polynomial as well as the points of the detected frequency during the calibration process. The third order polynomial, that describes the fitted surface, is used to transform the frequency that the reader has calculated into the sensed input

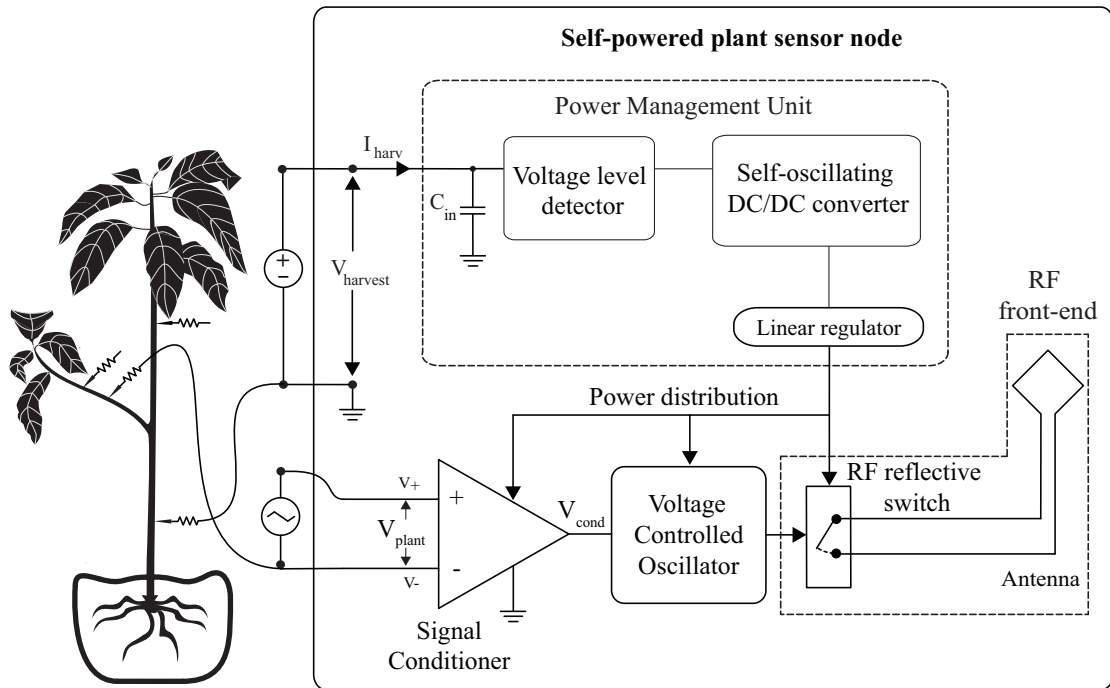


Figure 5.12: Setup of self-powered node during the calibration process.

voltage ( $V_{plant}$ ) taking into account the environmental temperature. Table ?? indicates the Root Mean Square error of the manufactured battery-powered nodes as resulted from the least squares fitting for each node. The RMS calibration error for the self-powered nodes that were developed is 17 mV.

	Battery assisted nodes							
	#1	#2	#3	#4	#5	#6	#7	#8
RMS								
Calibration error (mV)	6.01	14.39	10.06	14.05	6.57	26.99	17.57	22.80
Relative to full-scale (500 mV) %	1.2	2.8	2.0	2.8	1.3	5.3	3.5	4.5

Table 5.4: Calibration error for the eight battery-powered nodes which have been constructed.

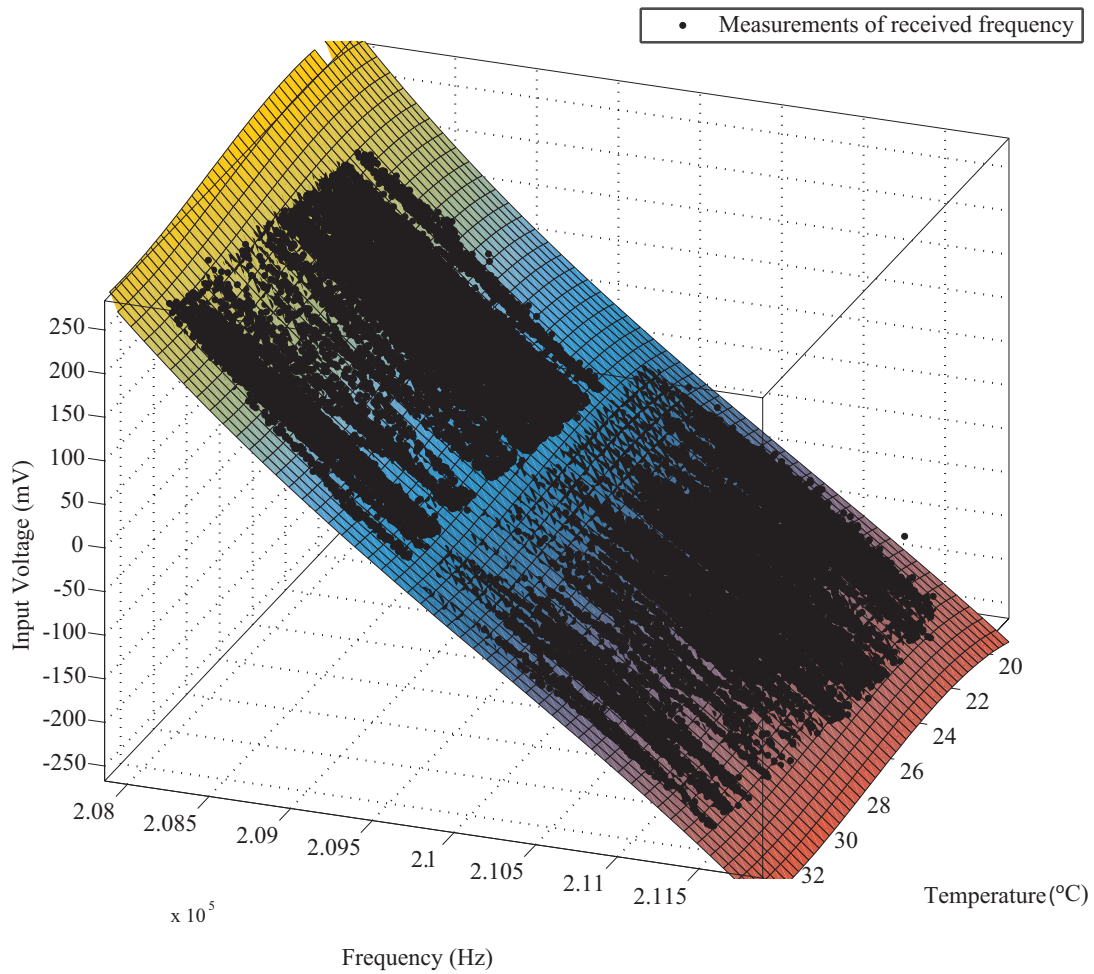


Figure 5.13: Measurements of calculated frequency for different  $V_{plant}$  inputs for various environmental temperature conditions laying on the fitted surface for Node 1 of the battery-assisted network.

## 5.4 Plant Signal Measurements

Figure ?? illustrates the experimental measurements of the electro-physiological signal generated by an Avocado plant during 28/9/2014 - 5/9/2014, which have been acquired by the biological powered WSN node and received by the Reader through the backscatter communication link, as well as the corresponding values of ambient temperature, air humidity and incident solar irradiation. The AP signals generated shortly after the irrigation events are also illustrated, indicating that plant depolarization takes place for a few minutes after the irrigation event

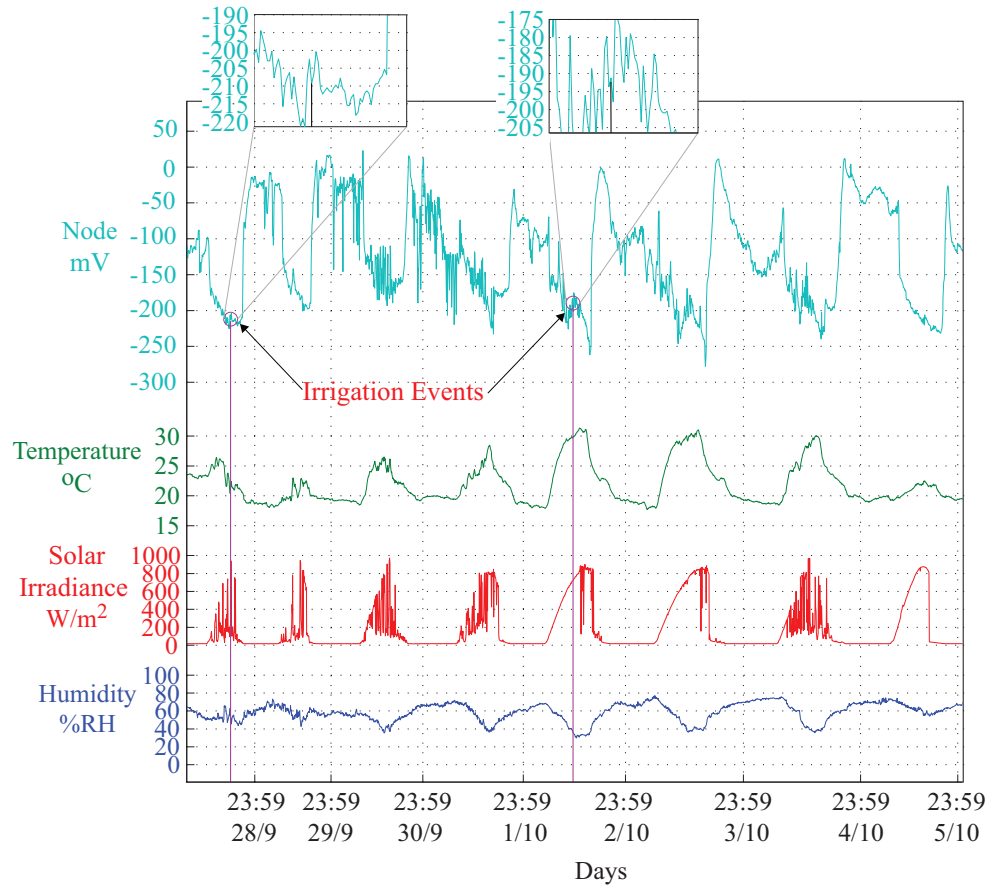


Figure 5.14: Measurements of the self-powered signal acquisition node. The insets illustrate the electrical response of the plants during irrigation.

as described in [? ]. Furthermore, significant plant response is exhibited during incidence of solar irradiation as comprehensively described in [? ? ]. The measurements that were extracted from a batch of Avocado plants using the eight battery-powered WSN nodes are illustrated in Fig. ?? . The day-night cycles of the plants are clearly indicated in these waveforms.

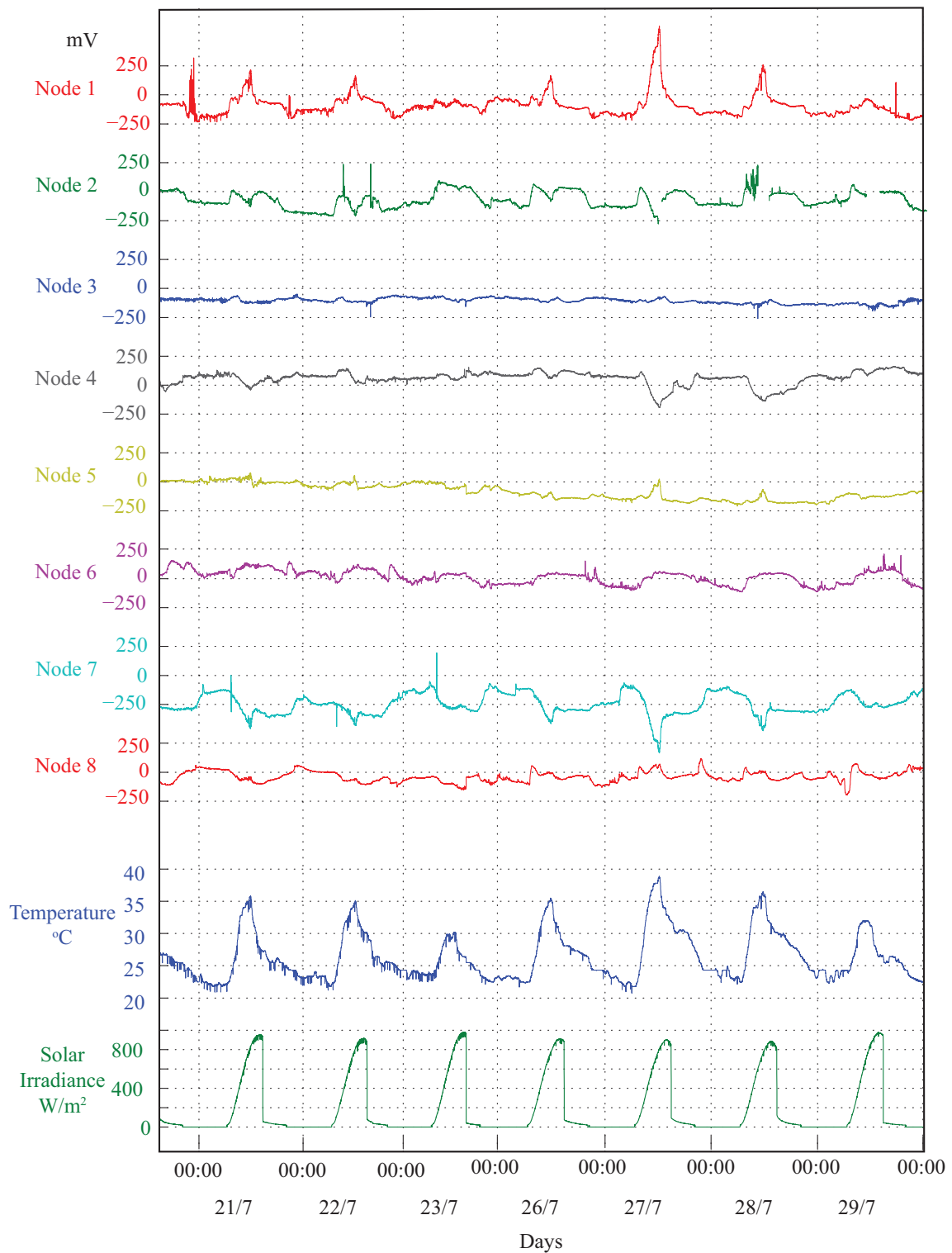


Figure 5.15: Measurements acquired by the plant signal acquisition network comprised of eight nodes and the corresponding plots of ambient temperature and solar irradiation.

# Chapter 6

## Conclusions

As the investigation of the micro-climate dynamics of crops has been the center of scientific research, WSNs have played a key role in monitoring essential environmental parameters that affect the micro-climate conditions. The biological electrical signals that are generated by the plants have been proven that are closely related to these conditions. In this context, the electrical signals generated by plants have been correlated in the past with their environmental conditions, as well as other forms of external stimuli, such as pollination, watering etc. However, due to the lack of appropriate sensing technology this acquisition of the plant signals has not yet been incorporated in precision agriculture schemes. Filling this gap, the proposed WSN node enables the implementation of low-cost, large-scale and fully-autonomous Wireless Sensor Networks. Particularly, it is an ultra low power design which is able to harvest, sense and transmit the plant bio-electrical signals employing analogue scatter radio principles that do not require amplifiers or mixers which conventional wireless architectures utilize (ZigBee, etc.). The prototypes that were developed were employed to demonstrate a wireless acquisition of this type of signals from multiple plants.

Further investigation of the concept could be performed. Research towards the optimization of the efficiency of the power management unit will increase the transmission time for a given input capacitance. Particularly, research steered towards power management architectures that compromise a cold-start sub-system as well as an efficient main power converter will increase the operational duty cycle. With much more energy available, the number of the nodes that a network based on self powered nodes could support will augment. Moreover, further investigation should be conducted towards the optimization of the node's RF front end. The integration of the antenna with the RF switch will provide increased received SNR that results in further increase of the communication range.

# Photographs



Figure 1: Prototype of the self-powered node.

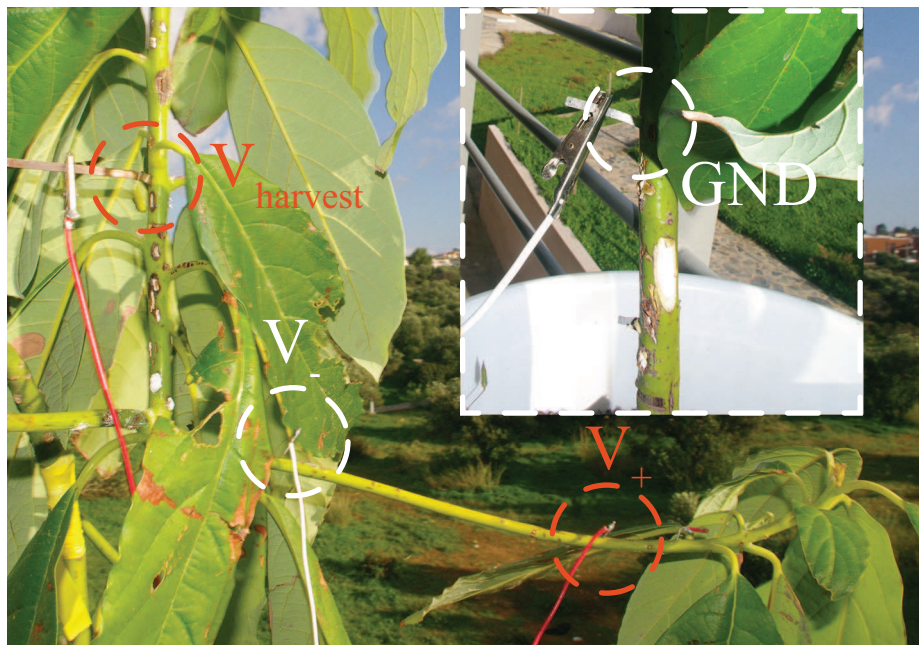


Figure 2: Electrodes setup during the experimental measurements for the self-powered node.

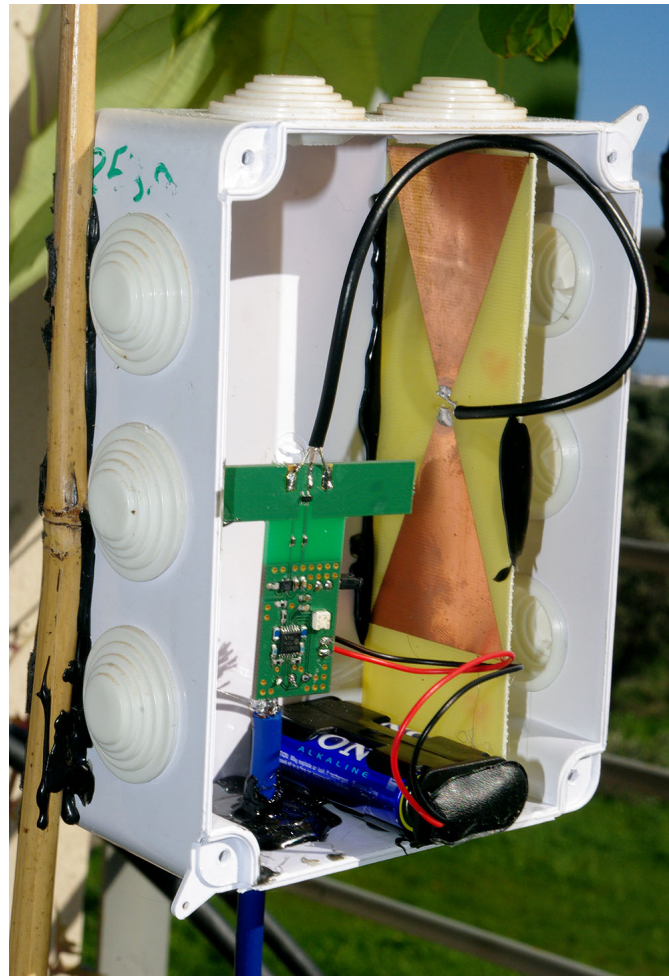


Figure 3: Prototype of the battery-assisted node.

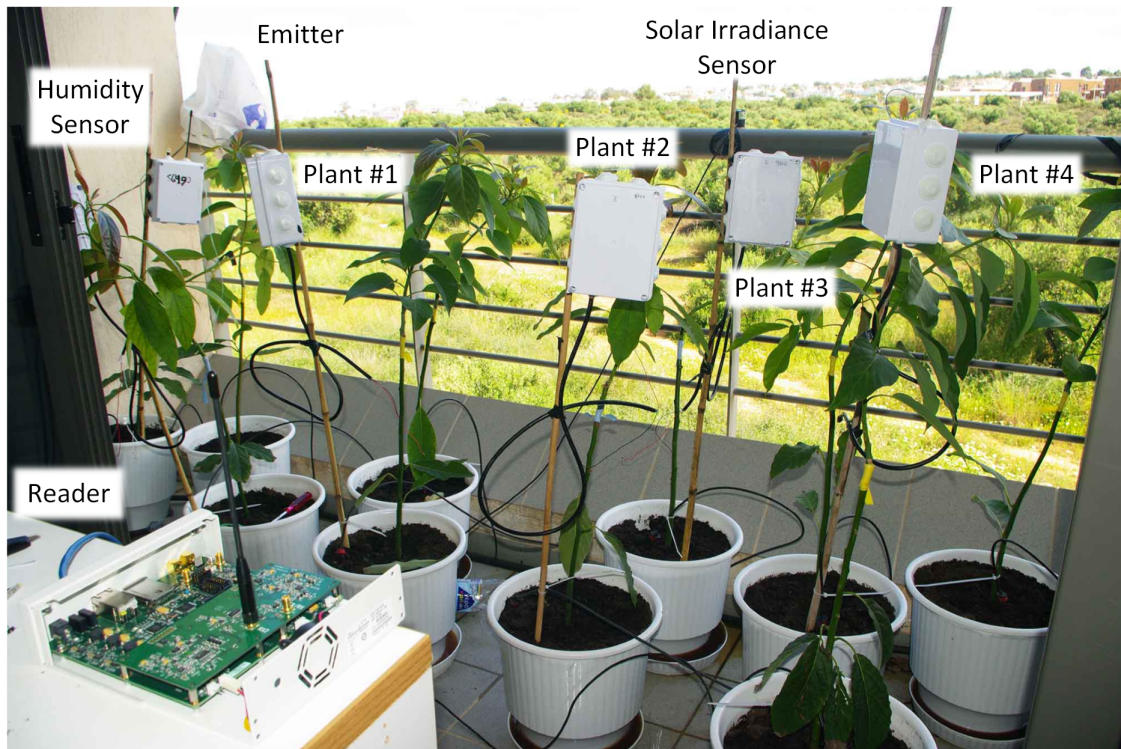


Figure 4: Experimentation setup for the wireless plant signal acquisition with 4 battery assisted nodes attached on 4 plants.

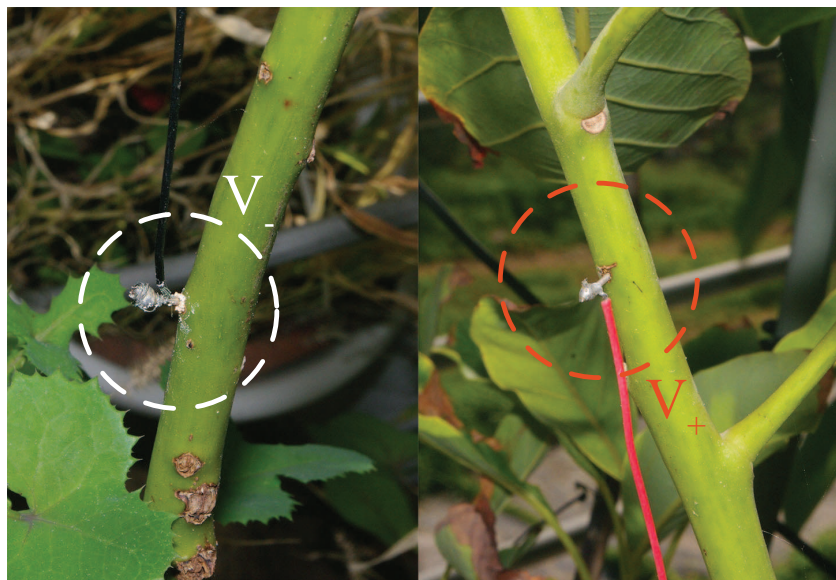


Figure 5: The  $V_+$  and  $V_-$  Ag pin electrodes attached on the avocado plant.